Bulletin of Earthquake Engineering
https://doi.org/10.1007/s10518-026-02492-y

ORIGINAL ARTICLE

Sliding joint masonry infill with deformable contact material: interaction with the RC frame and design guidelines

Simone Pelucco[1] · Riccardo R. Milanesi[2] · Paolo Morandi[2] · Valentino Bolis[1] · Andreas Stavridis[4,3] · Guido Magenes[5] · Marco Preti[1]

Received: 18 February 2025 / Accepted: 26 April 2026

Abstract
The seismic vulnerability of traditionally constructed masonry infilled frames has been repeatedly highlighted in post-event surveys, as well as by experimental and numerical studies. Infill walls with sliding joints can improve the seismic response of these structures. The paper describes some design equations derived from a parametric numerical analysis focusing on the interaction between the RC frame and the masonry infill with sliding joints. A previously proposed analytical model, able to predict the lateral strength contribution and the column shear overload due to the infill-frame interaction, is here extended to widen its field of application to walls with column-to-infill contact material characterized by and elastic response instead of an elastic-plastic one. A previously validated finite element modelling method is used to conduct a parametric study examining the role of the key design parameters of ductile masonry infill walls that implement sliding joints. The main model parameters are calibrated using data obtained from a previous comprehensive experimental campaign. A comparison of numerical and experimental results is also reported. The influence of different infill-frame contact material stiffnesses is analysed together with other design parameters, such as the bay length, the masonry properties, the layout of sliding and contact joints.

Keywords Infill-frame interaction · Innovative infills · Ductile infills · Sliding joints · Design parametric analyses · Design formulation

✉ Marco Preti
marco.preti@unibs.it

[1] D.I.C.A.T.A.M, University of Brescia, via Branze 43, 25123 Brescia (BS), Italy

[2] Eucentre, Via Ferrata 1, 27100 Pavia (PV), Italy

[3] University of Patras, 26504 Rio, Greece

[4] University at Buffalo, 224 Ketter Hall, NY 14260 Buffalo, USA

[5] D.I.C.Ar, University of Pavia, via Ferrata 3, 27100 Pavia (PV), Italy

Published online: 22 May 2026

1 Introduction

The seismic vulnerability of RC frames with traditional masonry infills has been consistently observed in several post-event surveys (Manzini and Morandi 2012; Parisi et al. 2012; Fragomeli et al. 2017; Fikri et al. 2019). These surveys have identified various issues, including the in- and out-of-plane interaction during seismic activity (Fig. 1a), the significant impact on the overall seismic behaviour of structures, and the structural damage resulting from the interaction between masonry panels and the bounding structural members (Fig. 1b).

These issues have recently prompted researchers and practitioners to develop innovative infill solutions, which can generally be categorized into three groups depending on their in-plane response (Preti 2024): i) enhanced infills (Valluzzi et al. 2014; Verderame et al. 2019; Furtado et al. 2021; Pohoryles and Bournas, 2020) provided with additional strength and/or ductility, ii) infills decoupled from the frame (Binici et al. 2019; Marinkovic and Butenweg, 2019), and iii) in-fills with ductile panels (Preti et al. 2012; Totoev and Al Harthy 2016; Morandi et al. 2018; Cheng et al. 2020; Milanesi et al. 2022) with reduced lateral stiffness and strength.

This study focuses on infills featuring sliding joints, which can be considered ductile panel infills. Infills with sliding joints involve partitioning of the infill panel into sub-panels separated with surfaces along which the sub-panels can easily slide when the frame bay deforms in-plane (Fig. 2). Previous studies have successfully utilized both vertical and horizontal sliding joints. These infills reduce the interaction between the masonry panel and the reinforced concrete (RC) members compared to traditional masonry walls, mitigating the damage of the bounding frame by preventing the formation of strong diagonal struts.

The relative sliding of the sub-panels is activated under in-plane lateral loads when surfaces without cohesion and with a sufficiently low friction coefficient are introduced in the infill. These surfaces, adopted during the construction of a new infill, can also be introduced in existing infills (Preti and Bolis 2017; Gao et al. 2024). Research results indicate that the sliding joints can be even more effective when the normal stress acting on them is reduced. This can be achieved when the infill-to-top beam joint, called "top joint" here, is filled with a soft material with negligible or low mechanical stiffness. Depending on the mechanical

(a) (b)

Fig. 1 (**a**) Infill damage and collapse due to in-plane and out-of-plane behaviour during the 2016 central Italy earthquake (Fragomeli et al. 2017); (**b**) Focus on the local shear cracking in an RC column due to the infill-structure local interaction (Parisi et al. 2012)

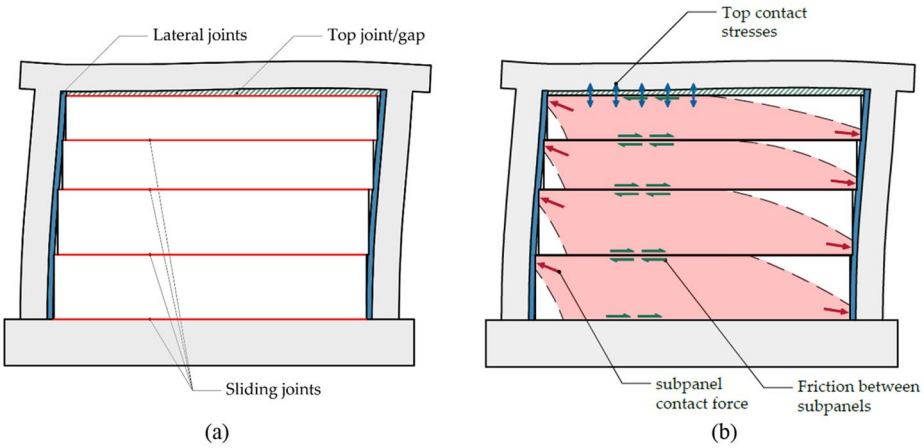

Fig. 2 (**a**) Schematization of the sliding joint infill solution and (**b**) representation of the main mechanisms that govern the behaviour

properties of the material used, this may result in either a top gap layout or a deformable top joint layout, as show in Fig. 2.

The efficiency of sliding joints can be improved by adopting a deformable contact material at the column to infill interface. Such contact material can absorb the required local deformation between the frame and the sub-panels and therefore reduce the contact forces. This contact material can have either a low mechanical stiffness (Morandi et al. 2018) or a low-strength ductile response (Preti et al. 2015).

The infills considered in this paper utilize an elastic, deformable, contact material in the vertical joints between the infill and the bounding RC frame columns ("lateral contact joints" in the following). This is an alternative to previously tested sliding joint infills (Preti et al. 2012; 2015; Gao et al. 2018; 2024) featuring lateral contact joint with an elastic-plastic response (yielding contact joints) that, for example, can be made of wooden boards. In the latter the sub-panel masonry is protected from crushing thanks to the limitation of local contact stress intensity by means of the yielding of the contact material, which needs to have a yielding strength in compression (cap plastic strength) lower than the masonry compressive strength. The assessment of the role of an elastic deformable contact material widens the range of applicability of the sliding joint system, by allowing the use of various low stiffness material, for example elastomeric or foam ones, as lateral contact joint. Some benefits are the reduction of the infill thrust on the column, the mitigation of pinching in the hysteresis and the possible adoption of the contact material as filler in the "top joint" thanks to its low stiffness. An example of the infill layout under consideration is reported in Fig. 3 (Morandi et al. 2018). The elastic deformable contact material purpose is to limit the interaction forces between the panel and the frame column. Without a cap plastic strength for the lateral contact joint, these forces could exceed the local strength of the masonry panel, inducing undesired and premature local crushing in the case of a weak infill. The lateral contact joint stiffness must therefore be designed according to the masonry's mechanical properties and geometric dimensions, as set out in the equations proposed in the present study.

The study also focuses on the effect of the mechanical properties of the material filling the top joint between the infill and the beam, which can be realized for example with a soft

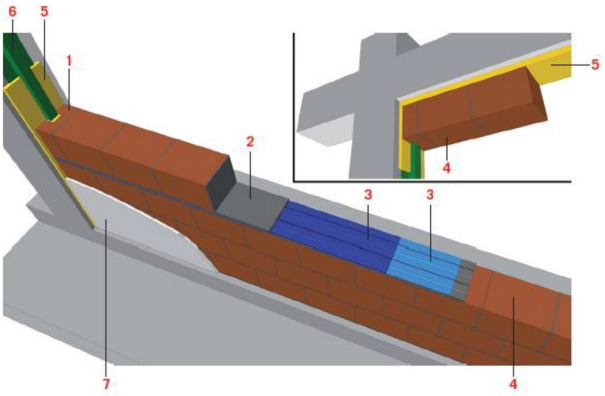

Fig. 3 Details of the experimental masonry infill with sliding joints: 1. C-shape units; 2. mortar bed-joints; 3. sliding joints; 4. clay units; 5. contact joints; 6. shear keys; 7. plaster (Morandi et al. 2018)

elastic material like the lateral contact joint. In fact, the top contact joint may exert a vertical confining action on the infill during the sway mechanism, particularly at large interstorey drift, which may jeopardize the subpanel sliding along the horizontal joint, with consequent shear overstress of the masonry panels (Preti et al. 2012). On the other hand, Gao et al. (2024) show that good results can be obtained despite this confining action, in a test on a retrofitted existing infill. Thus, an investigation is needed to shed light on this aspect.

The paper discusses the effect of some construction details (namely lateral and top infill frame contact joint stiffness, number of sliding joints, masonry compressive strength, infilled bay length) in the in-plane response of ductile infill with sliding joints, extending the parametric analysis presented by Bolis et al. (2017) to account for such details. The potential to predict in-plane seismic response of such infill solution using design-based equations is also discussed, proposing simple equation to assess both the beneficial in-plane contribution of the infill to the frame storey lateral resistance and the unfavourable column shear overload due to such infill-frame interaction. To this end, an extension of the analytical approach presented by Preti et al. (2019) is proposed, specific for infills having elastic soft material contact joints (#5 in Fig. 3) with elastic response instead of yielding ones, and this aspect represents the study's primary innovation, with the goal of developing a practical formulation to be incorporated into design guidelines. The research employs a previously validated finite element model methodology (Bolis et al. 2017; Stavridis and Shing 2010) adopted to model the detailing alternatives proposed in the experimental investigation reported in Morandi et al. (2018), whose full-scale test specimen is here used as reference case study. To support the calibration of the case study model, this paper reports several originally unpublished experimental local deformation measurements, while specimen details, material properties, test procedures, and in-plane seismic response are provided by Morandi et al. (2018).

2 Parametric analysis: case study and adopted modeling

2.1 Numerical modeling scheme

The behaviour of the case study specimen is modelled with a detailed FE modeling scheme, which combines the smeared- and discrete-crack approaches (Stavridis and Shing 2010) to

capture the different failure modes of infilled RC frames, including the mixed-mode fracture of mortar joints, the crushing and cracking of the masonry units, and the flexural and shear failure of RC members. The modeling schemes used for the RC members and the masonry panels are illustrated in Fig. 4.

The modelling scheme for RC members uses a module of four triangular smeared-crack elements connected with four, diagonally-placed, double-noded, interface elements, as illustrated in Fig. 4a. This mesh allows the development of discrete cracks at angles of 0°, 90°, and θ, where θ can be close to 45° to represent diagonal shear cracks. The flexural steel is equally divided into eight truss elements at each interior location, and four truss elements along the external edges of an RC member. The total shear steel area at each location can be divided into two bars placed diagonally, in a zigzag pattern, across the horizontal interface elements alignment (Fig. 4a). This detail of the modeling scheme prevents the sliding along such horizontal interfaces, which is not a realistic failure pattern, and ensures that every potential discrete crack would cross the proper quantity of steel.

In the case of the masonry infill, the mortar joints are represented with zero-thickness cohesive interface elements. Hence, the material parameters for the continuum brick elements reflect the properties of a masonry assembly rather than those of the brick itself. The discretization is shown in Fig. 4b, in which each masonry unit is modelled with two rectangular continuum elements interconnected with a vertical interface element to allow the vertical splitting. Details about the modeling scheme, constitutive models, and calibration procedure can be found in Stavridis (2009).

This detailed FE modeling approach for infilled frames has been implemented in FEAP (Taylor 2007) and extensively validated with experimental data from test specimens ranging from quasi-statically tested single-bay single-story frames, to multi-story multi-bay frames tested on the shake table (Stavridis and Shing 2010; Koutromanos et al. 2011; Redmond et al. 2016; Bolis et al. 2017; Bose et al. 2019). These specimens include non-ductile RC frames designed with the practice followed in California in 1920s, and ductile RC frames designed following the current Eurocode, Turkish, and Indian codes. Moreover, the specimens include solid masonry panels, and walls with window and door openings. The masonry units used in these studies range from strong solid concrete and clay bricks to hollow clay tiles found in the US, the extremely weak autoclaved aerated concrete units (AAC) used in India and the hollow masonry units used in Italy.

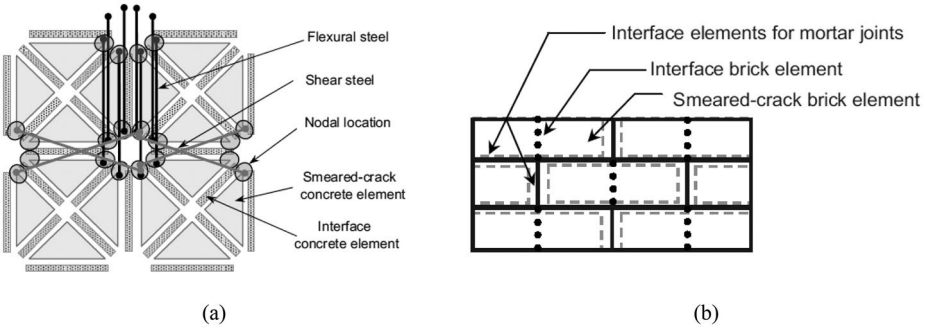

Fig. 4 Finite element discretization (reprinted from Stavridis and Shing 2010) of the RC members (**a**) and masonry infill panel (**b**)

The modeling approach has been extended to simulate the response to in-plane loads of RC frames with sliding joint infills by Bolis et al. (2017). As shown in Fig. 5, a combination of discrete and smeared crack elements in series is used to capture the behaviour of the deformable mortar that is used to form the lateral and top contact joints. The response of those joints under compressive stress (normal to the contact surface) is governed by the properties of the smear crack element. The sliding and possible detachment at the vertical interface between the masonry panel and the column is simulated by an interface element. This element (Lotfi and Shing 1991) remains elastic in compression but can simulate the mixed-mode fracture of quasi-brittle materials. Similar interface elements are adopted to model the horizontal sliding joints separating the subpanels.

2.2 Reference test structure

The case study full-scale reference structure (Morandi et al. 2018), shown in Fig. 6, had a bay length of 4.22 m and height of 2.95 m, while the reinforced concrete members had a square section with a base/height dimension of 350 mm. The RC frame was designed to represent actual structures with current ductile reinforcement detailing, while the infill included sliding joints featuring original design elements, developed based on the conceptual framework proposed by Preti et al. (2015). The infill was divided into four horizontal subpanels that could slide relatively to each other over specifically designed sliding joints made of plastic material. Additionally, a specifically designed cementitious based material deformable mortar of 25 mm thickness was used at the interface between the masonry subpanels and the reinforced concrete members to reduce the stress concentration, both on the columns and top beam infill-frame interfaces. The material of the interface mortar joints was selected because it offers acoustic and thermal insulation, along with good compression performance. Compared to general purpose mortar, this material has a lower elastic

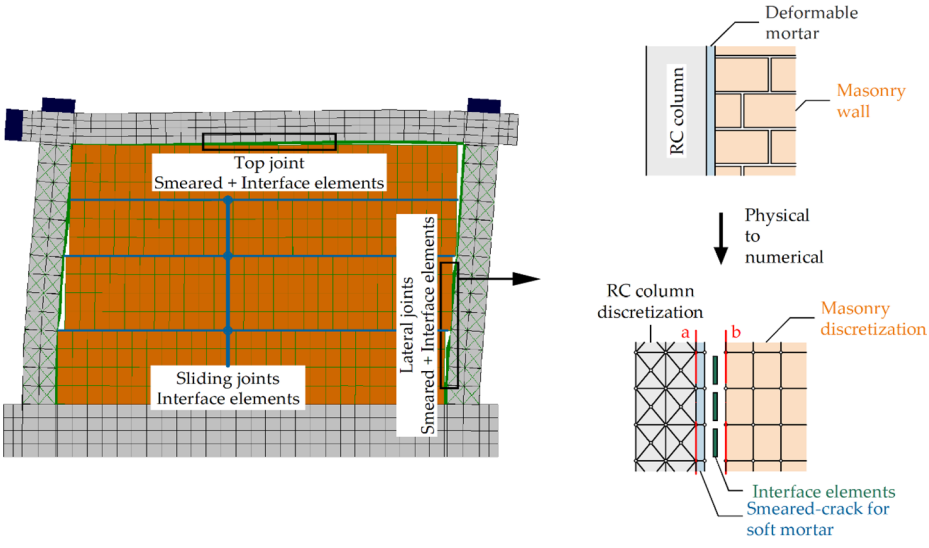

Fig. 5 (**a**) Infill frame mesh and detail of the sliding and contact joints; (**b**) detail of the contact joint modeling

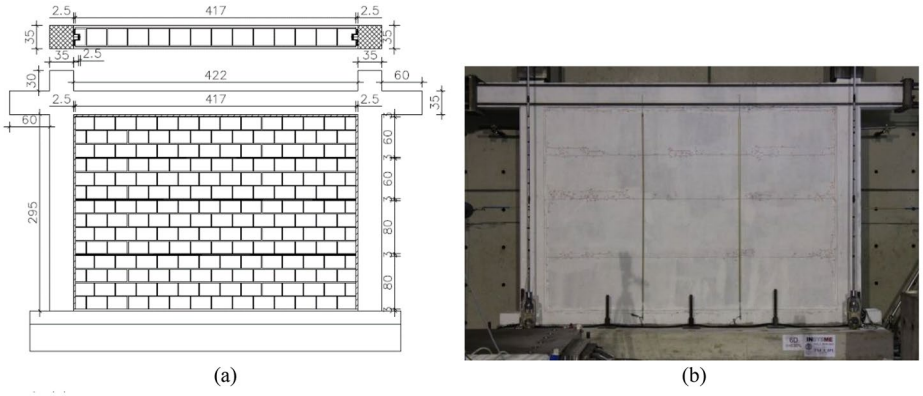

Fig. 6 (**a**) Layout of the fully-infilled specimen (TSJ1, Morandi et al. 2018) and (**b**) damage pattern after in-plane cyclic loading up to 3% interstorey drift (Milanesi 2016)

modulus and can handle greater strain without losing strength. The mechanical properties are discussed in the following sections. Further details are reported in Morandi et al. (2018). The unreinforced masonry of the subpanels consisted of 250 mm thick vertically perforated clay units with general-purpose 10 mm thick mortar in bed and head joints. The infill surfaces were plastered with a fibre reinforced mortar layer, with a reduced thickness at the sliding joints. During the test, the displacements and deformations were monitored using 45 displacement transducers (linear potentiometers) as shown in Fig. 7a. Figure 8a illustrates the force-displacement hysteretic curves and their respective envelopes for each cycle of the fully infilled configuration (TSJ1).

Transducers numbered between 30 and 44 were positioned at the panel/column interface to measure the compression of the deformable mortar joint or the detachment of the subpanel from the reinforced concrete columns (Fig. 7b). Each subpanel was equipped with 2 potentiometers at each masonry/column interface, one at the top and one at the bottom of the subpanel.

The damage observed during the in-plane tests included horizontal cracks in the plaster at the sliding joints and partial detachment at each panel to column interface. These are indicative of the activation of the sliding mechanism at levels of drift as low as 0.20%. At drift levels of 1.00–1.25% sub-horizontal flexural and minor diagonal cracks developed in the upper and lower sections of the reinforced concrete columns due to in-plane deformation of the structural frame. Then, at a drift ratio of 2.00%, small areas of plaster at the corners of the subpanels detached as shown in Fig. 8b. Finally, spalling of the concrete cover occurred at the bottom of the columns at 3.00% drift.

2.3 Calibration of the material parameters

The values of the modeling parameters are selected following the methodology suggested by Stavridis and Shing (2010) for the RC frame and masonry infill, while the recommendations by Bolis et al. (2017) are used to calibrate the sliding joints. All the model parameters are physically based and derived by experiments on material or sub-assembly specimens tested by Milanesi (2016), and/or well-established values according to the procedure proposed by

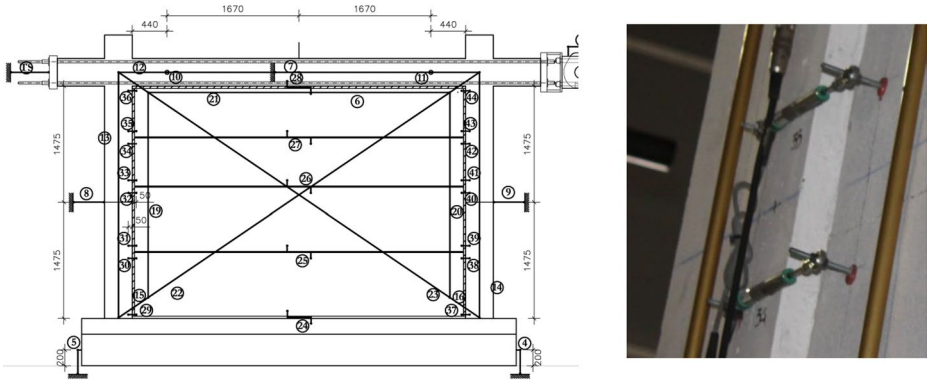

(a) (b)

Fig. 7 (**a**) Sketch of the linear potentiometer installed in the specimen during the in-plane cyclic test; (**b**) Detail of the potentiometer 34 and 35 installed to monitor the subpanel/column local interaction

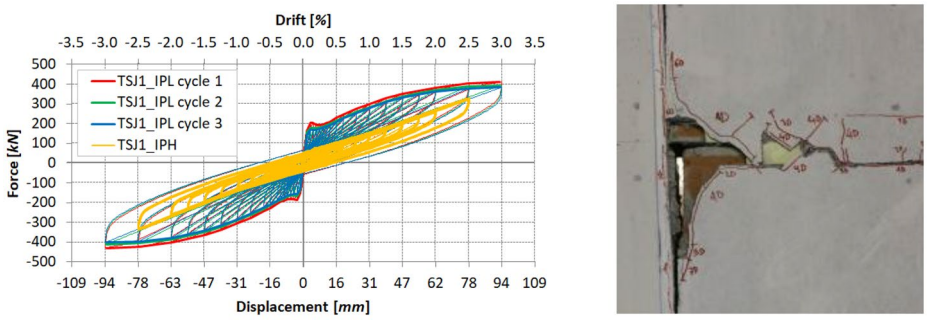

(a) (b)

Fig. 8 Experimental force-displacement cyclic and envelopes curves of specimen TSJ1 (Morandi et al. 2018) (**a**) and focus of the masonry/column interface joint at the max imposed in-plane drift of 3.00% (**b**). IPL (in-plane low velocity) and IPH (in-plane high velocity) refer to cycles performed at low and high velocity, respectively, with the latter performed after the sequence of cycles at low velocity. The applied velocity is not constant and is reported in Morandi et al. (2018) and Milanesi et al. (2017)

Stavridis (2009) and Stavridis and Shing (2010). The main and most influencing parameters are obtained from the mechanical characterization test described in the following.

The smeared-crack elements simulating the contact joints are calibrated to have a simplified linear response equivalent to the test data. The deformable mortar working as contact joint was experimentally characterized in various ways: by testing mortar prisms (160×40×40 mm) under longitudinal compression, by investigating the influence of the specimen dimension using mortar pads (25×300×70 mm), and by replicating the entire interface region on the column (see Fig. 3) for a height of 190 mm (equal to the masonry block height), including the steel omega element and the C-shape clay unit and two mortar pads (25×190×70 mm each) on the sides of the steel omega shear key. The results, shown in Fig. 9a, underscore the variability of such mortar response with the test set-up and the need to make assumptions regarding the compressive behaviour of this material. The results of the three types of tests are reported: “Mortar prism”, “column-pad” and “complete system”.

The tests have been always conducted through a compression only monotonic loading. For the "mortar prism" specimen the mortar has been casted in a steel framework, in compression only in the direction of 160 mm to study the possible influence of the boundary condition. The "column-pad" specimen is a portion of the precast mortar interface joint (see Morandi et al. 2018, for the construction process) tested in compression within two rigid thick steel plates. In "complete system", the specimen includes the precast column pads, the steel shear keys and adjacent clay units, to capture possible confinement on the deformable mortar joints due to the mutual interaction among elements, which may restrain its transverse deformation. Because the additional components were far stiffer than the mortar joints, strain remained concentrated in the deformable material. The load has been transferred through rigid thick steel plates.

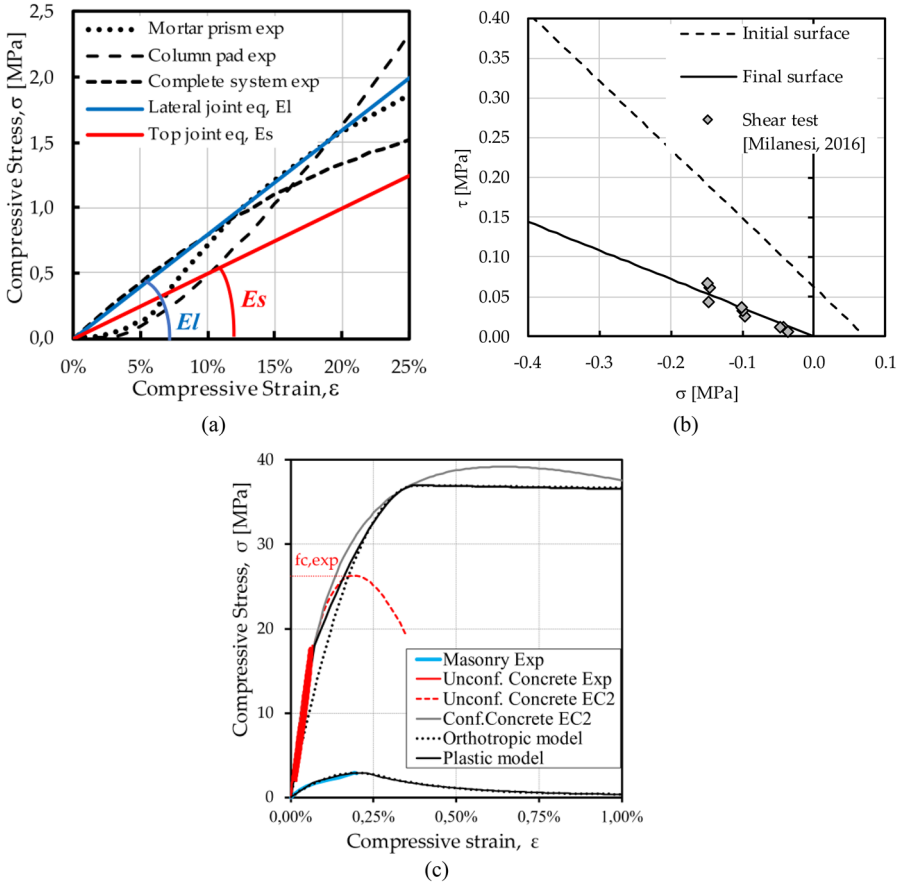

Fig. 9 Representation of the numerical model parameter calibration: (**a**) Experimental (exp) vs simplified equivalent (eq) stress-strain behaviour under compression of the deformable mortar in the contact joints; (**b**) Experimental vs simplified equivalent shear-normal stress behaviour for the sliding joints; (**c**) Experimental vs numerical stress-strain behaviour under compression of the concrete and masonry materials (smeared crack orthotropic and plastic model curves are reported for both concrete and masonry). The analytical concrete prediction of the full stress-strain relation of confined and unconfined concrete follows Eurocode 2 (EC2 - CEN 2004) with the confined concrete parameters derived according to Mander et al. (1988)

The results, shown in Fig. 9a, reveal that at low strains the pad specimens behave more flexibly, while at higher strains the test curves tend to diverge. The numerical parameters were calibrated so that the model predictions agree closely with the experimental results. The elastic modulus of the deformable mortar for the lateral contact joints (*El*) is selected to obtain a stress-strain curve that is secant to the experimental curve within the strain range of 15–20% (see the blu linear response in Fig. 9a). This range corresponds to the peak strain level observed in the test specimen at a drift level approximately equal to 2.0% (see Fig. 12). A similar approach is applied to calibrate the top joint deformable mortar elastic modulus (*Es*) but considering a lower strain demand during the test derived by evaluating the vertical displacement of the beam in the deflected configuration.

The interface elements representing the mortar and sliding joints are calibrated by aligning the initial and residual yield surface with the shear tests of the masonry triplets (Figs. 9b and 10b). As for the sliding joints, the model matches the characterization test without the plaster cover, thus the initial and final yield surface coincide given the negligible cohesion. No characterization tests on sliding joints covered by plaster are available. Hence, in a second step of calibration refinement, the role of the reduced plaster thickness covering the sliding joints is described by the incremented initial yield surface reported in Fig. 9b, derived from the plaster contribution to shear resistance measured in shear test on masonry triplets with and without plaster (Fig. 10b).

The key modeling parameters are listed in Tables 1 and 2. The comparison between the calibrated concrete and masonry stress-strain behaviour under compression and the data from the material tests is shown in Fig. 9c.

2.4 Infilled frame experimental vs numerical response

The tested infilled frame experienced very limited damage. The plaster covering the sliding joints cracked along the plane of sliding joints and some very localized plaster detachment occurred at the subpanel corners. The model capability to capture the overall infilled frame behaviour and the local subpanel deformation is described in the following figures. Focus is made on local deformation at the lateral contact joint.

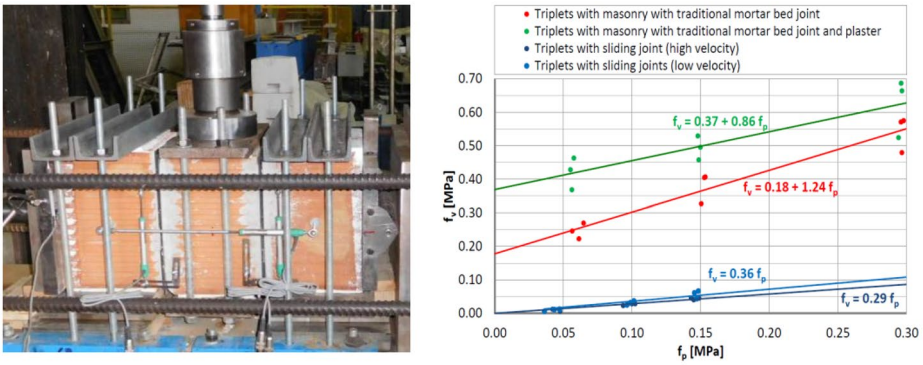

(a) (b)

Fig. 10 Picture of the tests of characterization set up (**a**) to determine the initial shear resistance of the masonry triplets and friction coefficient of the sliding joints (**b**) (reprinted form Morandi et al. 2018)

Table 1 Main parameters adopted for the smeared-crack elements (E and G = masonry elastic moduli; t = thickness; fc = compression strength; ft = tensile strength, 1 = strain at peak strength, 2 = strain at the onset of the exponential tail)

Material	SMEARED-CRACK ELEMENTS						
	E [MPa]	G [MPa]	f_c [MPa]	f_t [MPa]	1		t [mm]
Confined Concrete	25000	10417	37	1.0	0.0038	0.0038	350
Masonry	2600	1150	2.9	0.6	0.0020	0.0027	250
Deformable Mortar top	5	1.81	Unlimited	Unlimited	-	-	250
Deformable Mortar lateral	8	2.9	Unlimited	Unlimited	-	-	250

Table 2 Main parameters adopted for the interface elements (s_0 = initial tensile strength; $_0$ = slope of the asymptotes of the initial hyperbolic domain; $_r$ = slope of the asymptotes of the residual hyperbolic domain; r_0 = radius of the initial hyperbolic domain at the vertex; r_r = radius of the residual hyperbolic domain at the vertex; t = thickness of the interface element (further description can be found in (Bolis et al. 2017))

Material	INTERFACE ELEMENTS					
	s_0 [MPa]	$_0$ [-]	$_r$ [-]	r_0 [MPa]	r_r [MPa]	t [mm]
Bed joints	0.45	0.88	0.75	0.005	0.005	250
Brick head joints	0.70	1.00	0.80	0.280	0.210	250
Mortar vertical joints	0.90	0.86	0.75	0.005	0.005	250
Concrete joints	1.00	0.90	0.70	0.250	0.200	350
Lateral contact joints	0.00	0.80	0.80	0.00	0.00	250
Top contact joint	0.00	0.80	0.80	0.00	0.00	250
Sliding joints w/o plaster	0.00	0.36	0.36	0.00	0.00	250
Sliding joints w plaster	0.07	0.86	0.36	0.00	0.00	250

Figure 11 compares the experimental and numerical response of the tested infilled frame in terms of the base shear vs. lateral drift. To compare the results from the monotonic numerical analysis with the experimental data, the envelop curves for the positive (Exp+) and negative (Exp-) displacements from the cyclic test are presented. The overall response of the experimental specimen for drift larger than 0.5% is well captured by the numerical model, although the initial peak strength is underestimated. This initial difference is not significant, and it can be attributed to the plaster that covers the sliding joints adding resistance. However, the model can reasonably capture the progressive triggering of the sliding joints, which result fully triggered at 0.3% drift in both the model and test results.

The experimental and numerical local deformations of the lateral joints along the height of the frame are described in Fig. 12, in terms of average strain. The local experimental deformations are estimated under the assumption that the displacement measured by the potentiometer bridging over the lateral joints is equal to the lateral joint deformation. This assumption stems from the consideration that the masonry is significantly stiffer than the deformable mortar, by about two orders of magnitude. Hence, local strains are estimated by dividing measured displacement by mortar joint thickness. Negative measured values of strain indicate compression of the contact material, while positive values indicate fictitious tensile strain, which can indirectly quantify the gap opening at the sub-panel to column interface. In fact, no tensile connection is present either in the test specimen or in the numerical model. Since two potentiometers per subpanel measured the experimental deformation (at the top and bottom of each subpanel), a linear deformation profile of each

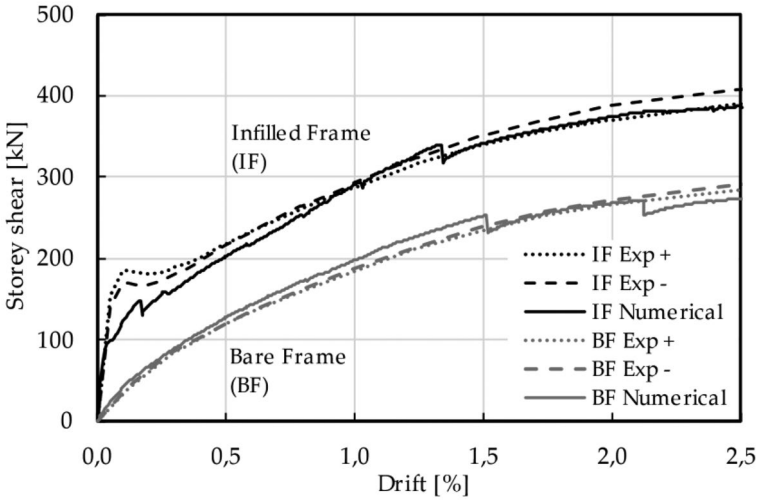

Fig. 11 Comparison of the storey shear-drift curves of the experimental envelope (Exp) and of the numerical model response for the infilled (IF) and bare (BF) case study frame

vertical joint is derived from the test data by interpolating between the two values. As for the test data, the numerical contact joint average strain is derived as the ratio of the relative displacement between the masonry node and the concrete node near the lateral contact joints (alignments "a" and "b" in Fig. 5b) over the contact joint thickness. It is important to note that, although the deformation of the lateral contact joint under compression is significantly lower, it remains of the same order of magnitude as the gap caused by the subpanel detaching from the column. This highlights the substantial deformation demands placed on the lateral contact joint, making its design a crucial factor in safeguarding the masonry corners of the subpanel from possible crushing. This is confirmed by experimental and numerical results.

Potentiometer n.38 (see Fig. 7a) has been damaged during the test, and some data are therefore missing, thus Fig. 12 does not report the experimental deformation of the bottom panel at the leeward column.

As shown in Fig. 12, the deformation profiles in the compression area are well captured. The accuracy of the model prediction is satisfactory for drift larger than 0.5%, after the full triggering of the sliding joints, and it slightly improves increasing the drift limit. Focusing on the compression strain peaks, in the range of drift from 0.5% to 2.5%, the average ratio, μ, of the numerical prediction and the experimental measured values is equal to 1.06, with a standard deviation, σ, equal to 0.29. Despite the limited effect on the practical application, it is worth noting that at drift demands lower than 0.2% the local deformation prediction is affected by the difficult interpretation of progressive triggering of the sliding joints, thus further modelling refinement is desirable when that range of drift is of interest. In detail, for drift ranges of 0.2 to 0.5%, 0.5 to 1.5% and 1.5 to 2.5%, the obtained values of μ and σ are 0.92 and 0.49, 1.06 and 0.32, 1.05 and 0.22, respectively. At a 2.00% drift, the maximum compressive strain is approximately 20%, justifying the strain level used for the calibration of the elastic modulus of the deformable mortar.

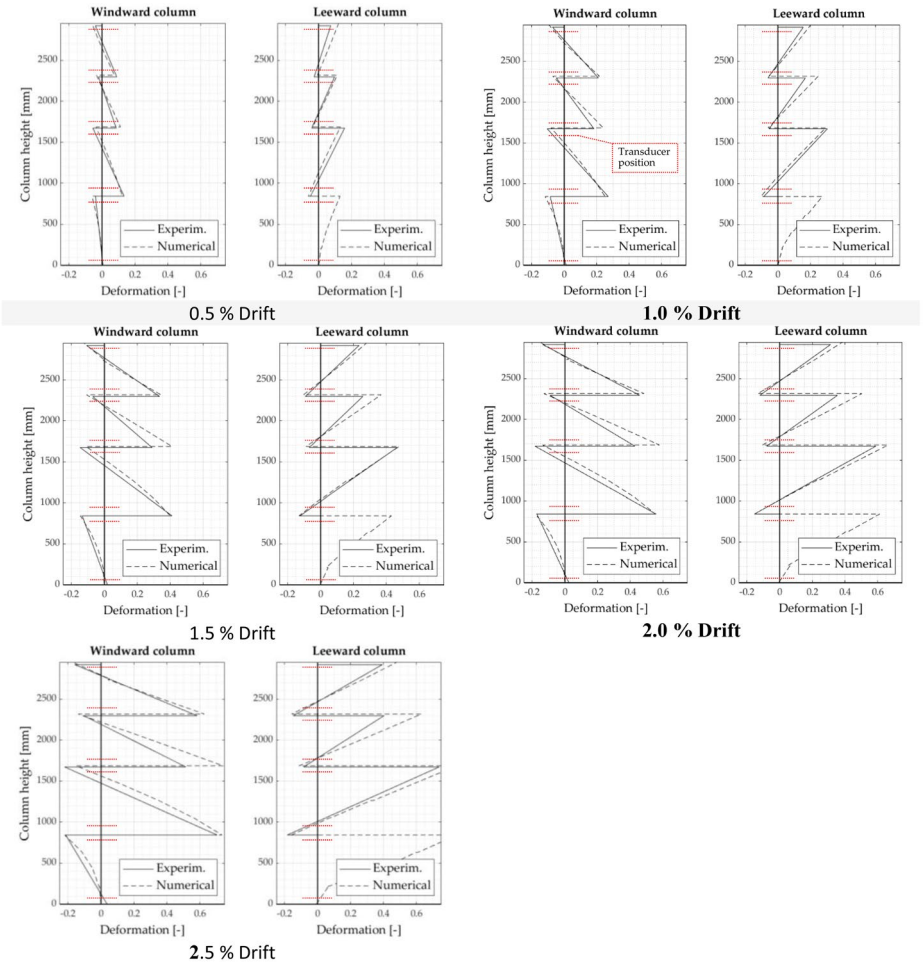

Fig. 12 Comparison of the experimental and numerical deformation profiles of the windward and leeward lateral joints at different drift levels from 0.5% to 2.5% (negative deformations are for compressive actions). Red dashed lines mark the position of the transducers measuring the local deformation at the column to infill interface

3 Parametric analysis: investigated parameters and results

The numerical model above described is used here in a parametric study to investigate the influence of several parameters related to both the infill geometry (i.e., the number of sliding joints and the bay length) and the mechanical properties of specific details. The base line (BL) structure considered in the parametric study is based on the test specimen TSJ1 discussed in a previous section. However, the BL model differs from the tested infilled frame in three details: (i) the top joint filler is assumed to have negligible stiffness and strength (top gap), (ii) a sliding joint is introduced at the base of the infill and (iii) no contribution of the plaster is assumed in the response of the sliding joints. In fact, the reduced plaster thickness over the sliding joints adds an initial strength, before the sliding joint triggering, which

was neglected in the parametric analysis, as the test showed it quickly vanished during the cyclic loading at low drift values. Figure 13 shows the comparison of the numerical model responses of the test structure, the bare frame structure, and the BL, including the case of the BL with plaster or with the top contact joint.

Regarding the material used in both lateral and top contact joints, five levels of stiffness are considered, assuming a perfectly linear elastic response. The investigation covers a range of material stiffness from 7 to 60 MPa, calibrated to hold significance in practical design. Starting from the scenario of a continuous panel with the sole base horizontal sliding joints and with deformable lateral contact joints, the study progresses to include an increasing number of intermediate sliding joints up to having one sub-panel per row of masonry blocks. The infill aspect ratio is analysed across a range of 3.2 to 6.1 meters of infill length (bay length). The masonry types were varied considering those taken in the prior parametric analysis described in Bolis et al. (2017). Additionally, the study examines responses to different lateral contact joint stiffnesses and aspect ratios in the case of top joint with an elastic modulus of 5.0 MPa and 25 mm thickness, as for the experimental specimen.

The details of the parametric analyses are described in Table 3 (BL with top gap) and Table 4 (BL with top contact joint). The comparison will be examined in terms of infilled frame storey shear versus interstorey drift, maximum shear action on the columns and drift at the onset of masonry crushing in the sub-panel corners.

Figure 14 illustrates the progressive reduction in the BL infilled frame lateral strength and initial stiffness by increasing the number of intermediate sliding joints. The most significant reduction occurs from one (J1) to two sliding joints (J2); but still, J2 shows anticipated crushing in the masonry subpanels corners, at drift values below 2%. A reasonable trade-off between infill frame mitigation and construction costs is represented by the solutions with three (J3 = Baseline) or four (J4) sliding joints (i.e. 4 and 5 sub-panels, respectively). In fact, starting from J3 corner crushing results prevented up to 2.5% drift, while additional joints

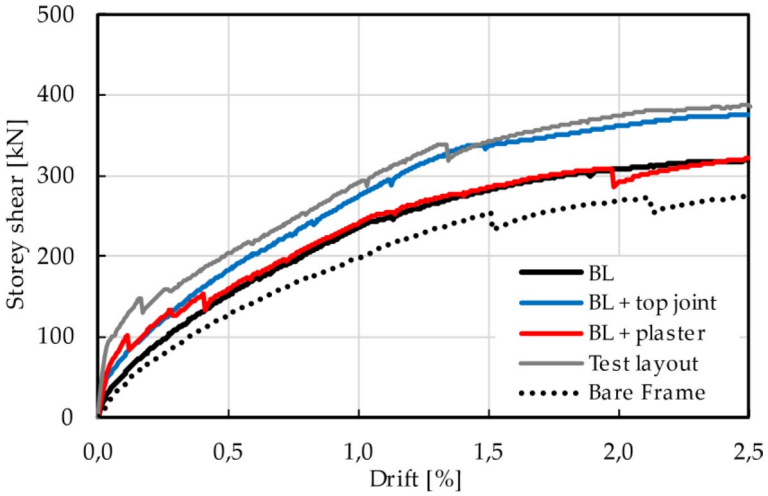

Fig. 13 Comparison of the storey shear vs drift in-plane response obtained from the numerical models for the infilled (test layout) and bare case study frame with that of the base line infilled frame model (BL). The results of the base line layout modified by introducing the top contact joint (BL + top joint) or the plaster cover over the sliding joints (BL + plaster) are also reported

with respect to J4 would escalate costs and construction time without a significant improvement in overall performance.

The overall in-plane response is not significantly influenced by the aspect ratio, as shown in Fig. 15a. Due to the deformation mechanism of the masonry panel, the infilled frame appears to be insensitive to variations in lengths; consequently, the storey shear curve can be assumed to remain practically unchanged regardless of the aspect ratio.

Figure 15b shows the influence of different masonry panel mechanical properties. Masonry properties slightly influence the response. The reason for this result is that the lateral joints are much more flexible than the masonry sub-panel material, causing most of the panel's deformation to occur there. Therefore, once masonry stiffness and strength reach a certain level, any further changes do not influence how the panel responds. Only with masonry materials characterized by very low stiffness and compressive strength, such as the "adobe" earthen masonry type, the response is modified and gets close to that of the bare frame.

Figure 16 illustrates the variation of the overall capacity curve as a function of lateral contact joint stiffness. For the BL with top gap (Fig. 16a), the lateral strength and stiffness increase with the stiffness of the lateral contact joint. For high drift demands, stiffer lateral contact joints can create local damage in the masonry panels highlighted by the partial strength drops, progressively anticipated as the lateral contact joint stiffness increases.

When the top joint is filled with the deformable mortar (BLf, Fig. 16b), the trend of lateral strength increase with the lateral contact joint stiffness is less pronounced. Sub-panel corner crushing still occurs depending on the stiffness of the lateral contact joints; the strength drops associated to such damage appear less pronounced when the top joint is filled compared to the case of the infill with top gap.

As shown in Fig. 17a, the stiffness of the top joint significantly influences the global in-plane behaviour. The overall strength increases together with its stiffness.

The length of the infilled bay and the consequent infill aspect ratio do not significantly influence the infilled frame response also for the BL with the top contact joint. A non-negligible trend of strength increase with the infilled bay length occurs for drift larger than 1.5% (Fig. 17b).

The influence of the investigated design parameters on the column shear action is reported in Fig. 18. Note that the shear action is quantified from the model at the column end sections as the integral of forces transmitted by the horizontal interface elements and the truss elements reproducing the stirrups (crossing the specific section - Fig. 4). Figure 18 reports such shear actions at the top of the windward column (W) and at the base of the leeward column (L) (dotted and solid lines, respectively), for four drift levels (0.5÷2.0%), showing the shear variation as a function of the investigated parameters reported on the abscissa.

The increase in the number of sliding joints results in a reduction in the shear action in the columns (Fig. 18a). The increase in the stiffness of the lateral contact joints leads to a progressive increase in shear action, both for the baseline with top gap (BL) and with contact joint (BLf), with little difference between the two conditions (Fig. 18b-d). The variation in the elastic stiffness of the top joint does not affect the shear action in the columns (Fig. 18c). The maximum internal action mainly occurs at the base of the leeward column.

The effect of the tested parameters on the infill damage is quantified in Fig. 19 in terms of local crushing at the corners of the subpanels. This condition is numerically identified when the first Gauss Point of the subpanel smeared crack elements adjacent to the columns

Table 3 Values adopted in the parametric study in the presence of the top gap at the infill to beam interface ("Param."=parameter considered in the parametric analysis; "code"=model title/name; "L"=infill length; "nj"=number of sliding joints partitioning the infill panel; "Mat."=masonry prism material; "E"=masonry elastic modulus; "fc"=prism lateral compressive strength; "ft"=masonry tensile strength; "t"=infill thickness; "top joint"= elastic modulus of top contact joint between the masonry and the beam; "Lat joint"=elastic modulus of the lateral contact joint between the masonry and the columns)

Param.	Code	Geometry		Material							
		L [m]	n_j	Masonry						Top joint	Lat joint
				Mat.	E [MPa]	f_c[MPa]		f_t[MPa]	t [mm]	Es [MPa]	El [MPa]
Baseline	BL	4.2	3	Hollow clay	2600	2.9	0.6		250	Gap	8.0
Lateral joint stiffness	El 7.5	4.2	3	Hollow clay	2600	2.9	0.6		250	Gap	**7.5**
	El 15										**15.0**
	El 30										**30.0**
	El 45										**45.0**
	El 60										**60.0**
Number of sliding joints	J0	4.2	**0**	Hollow clay	2600	2.9	0.6		250	Gap	8.0
	J1		**1**								
	J2		**2**								
	J4		**4**								
	J5		**5**								
	J6		**6**								
	J13		**13**								
Aspect ratio	L320	**3.2**	3	Hollow clay	2600	2.9	0.6		250	Gap	8.0
	L520	**5.2**									
	L620	**6.1**									
Masonry properties	AAC200	4.2	3	**AAC200**	**1600**	**1.8**	**0.25**		**200**	Gap	8.0
	AAC300			**AAC300**	**1600**	**1.8**	**0.25**		**300**		
	CU1*			**Solid Cu1**	**27579**	**23.44**		**4.82**	**190.5**		
	Mehrabi**			**Mehrabi9**	**15168**	**14.2**	**1.72**		**92.5**		
	Adobe*			**Adobe**	**79**	**0.62**	**0.23**		**120.1**		

*Bolis et al. (2017), **Mehrabi and Shing (1997)

Table 4 Values adopted in the parametric study in presence of the top contact joint at the infill to beam interface (the meaning of the parameters as in Table 3)

Param.	Code	Geometry		Material						
		L [m]	$\mathbf{n_j}$	Masonry					Top joint	Lat joint
				Mat.	E [MPa]	$\mathbf{f_c}$[MPa]	$\mathbf{f_t}$[MPa]	t [mm]	Es [MPa]	El [MPa]
Baseline	BLf	4.2	3	Hollow clay	2600	2.9	0.6	250	5.0	8.0
Lateral contact joint stiffness	El 7.5f	4.2	3	Hollow clay	2600	2.9	0.6	250	5.0	**7.5**
	El 15f									**15.0**
	El 30f									**30.0**
	El 45f									**45.0**
	El 60f									**60.0**
Top contact joint stiffness	Es 7.5f	4.2	3	Hollow clay	2600	2.9	0.6	250	**7.5**	8.0
	Es 15f								**15.0**	
	Es 30f								**30.0**	
	Es 45f								**45.0**	
	Es 60f								**60.0**	
Aspect ratio	L320	**3.2**	3	Hollow clay	2600	2.9	0.6	250	5.0	8.0
	L520	**5.2**								
	L620	**6.1**								

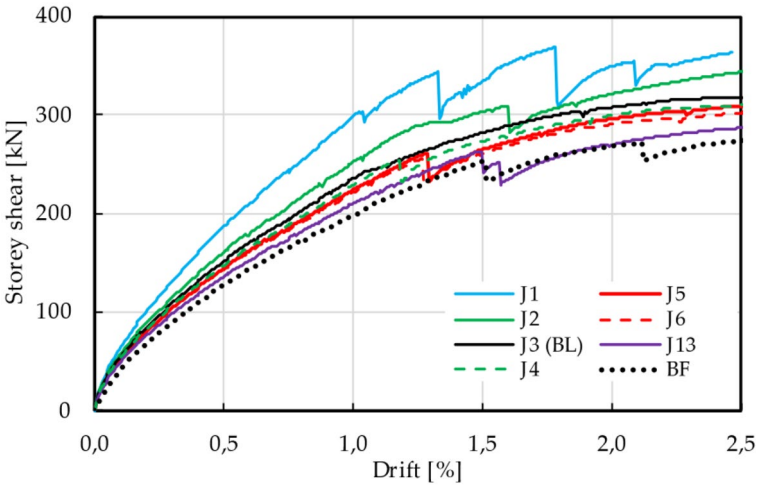

Fig. 14 Storey shear vs drift in-plane response of the infilled frame with a different number of the sliding joints and comparison with the bare frame (BF)

reaches the peak compressive strength. Figure 19a represents an example of the identification of the first local crushing for the case with a top gap and a stiffness of the lateral contact joints equal to 45 MPa; here, the crushing is visible in the upper corner at the windward side of the second subpanel, in the upper left Gauss Point (red "v"). The damage was monitored in the range of drift up to 2.5%. The parameter that mainly influences the activation of the

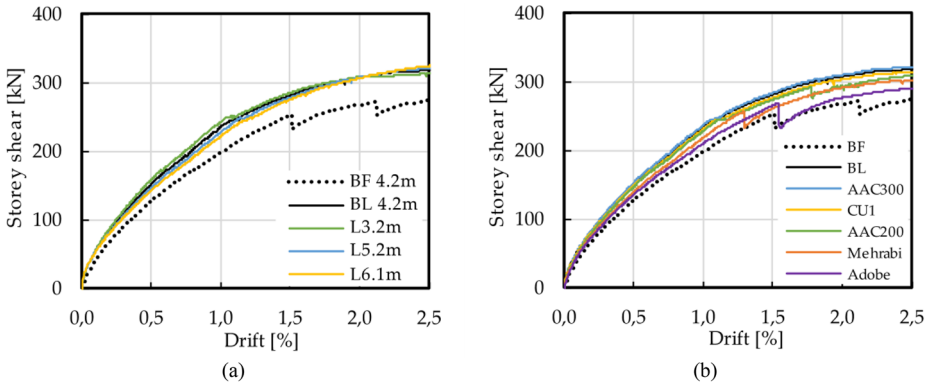

Fig. 15 Storey shear vs drift in-plane response of infilled frames of different bay lengths (**a**) or different masonry typologies (**b**) compared with the BL and the bare frame (see Table 3 for legend codes)

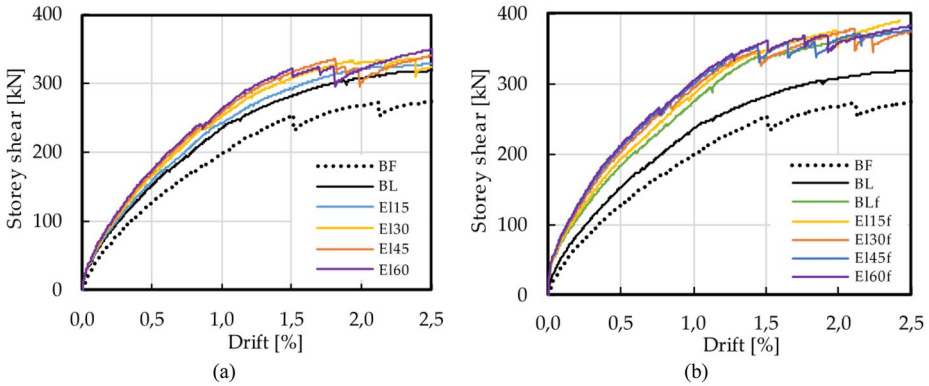

Fig. 16 Storey shear vs drift in-plane response of infilled frames with lateral contact joints of different stiffness compared with the BL (El8) and the bare frame. Results in presence of a top gap (**a**) or with the top contact joint of the same stiffness as in the test specimen (**b**) (see Tables 3 and 4 for legend codes)

local crushing is the stiffness of the lateral contact joints. Crushing occurs only for high lateral contact joint stiffness, starting with an equivalent elastic modulus of the contact material equal to 30 MPa and it is progressively anticipated at lower drift demands by increasing the lateral contact joint stiffness. No crushing was reached in the base line model with top gap (BL) or top contact joint (BLf) (neither for the different top contact joint stiffness investigated) and in infills of different lengths with and without the top gap.

4 Role of construction details and design implications

The parametric analysis shows the importance of some investigated construction details and highlights some design implications.

Starting with the preferable number of sub-panels separated by sliding joints, three sub-panels resulted sufficient to activate a ductile response, while a minimum of four is required

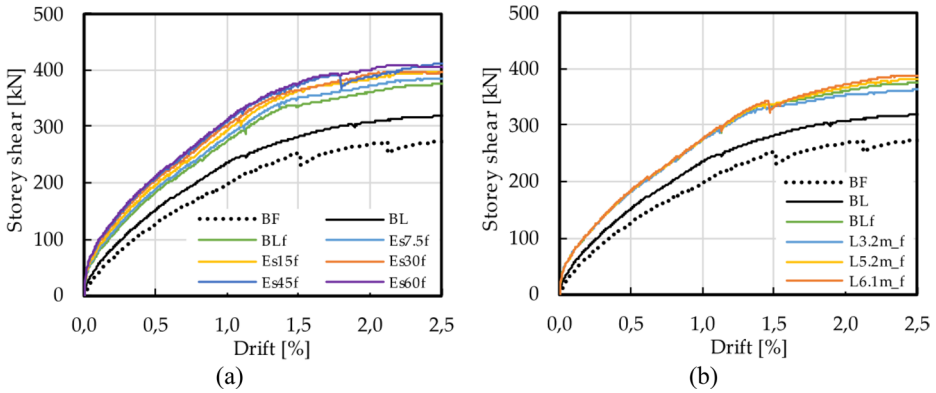

Fig. 17 Storey shear vs drift in-plane response of infilled frames with contact top joint of different stiffnesses and fixed bay length (4.2 m) (**a**) or for different bay lengths and fixed top joint stiffness (5 MPa) (**b**). The response of the base line infilled frames with (BLf - Es5f) and without (BL - L4.2 m) top contact joint and the bare frame (BF) are also reported

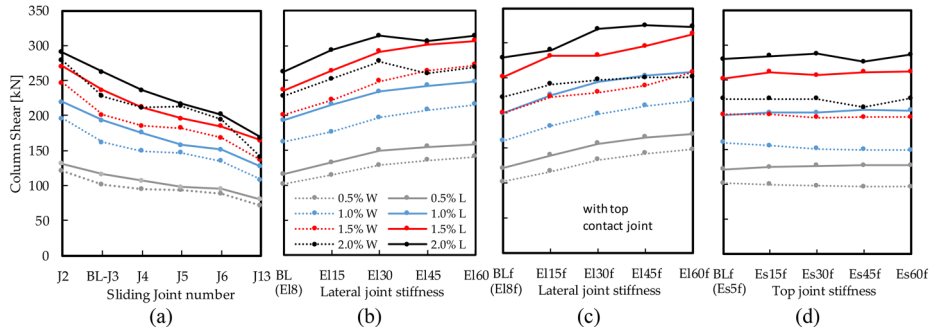

Fig. 18 Column shear at different Drift levels for infilled frames with different design details: response of the base line infilled frame (BL) by varying the number of sliding joints in the panel (**a**) or the lateral contact joint stiffness (**b**), in absence of top contact joint; response of the base line infilled frame with top contact joint (BLf) by varying the top joint stiffness (**c**) or the lateral contact joint stiffness (**d**). The shear action at the top of the windward column ("W") and at the base of the leeward one ("L") for different interstorey drift values is reported

to postpone the masonry crushing after 2.5% drift. More than four sub-panels do not significantly improve the in-plane behaviour. A uniform height for the sub-panels showed its efficiency, even if little differences do not significantly affect the response. The presence of a sliding joint at the base of the infill does not significantly modify the global response of the infilled frame, but it modifies the distribution of the shear action between the columns (Fig. 20): a regular mortar joint at the infill base instead of a sliding one produces lower shear action at the bottom end of the leeward column without significant increment of the maximum shear action on the windward one.

The contact of the infill with the top beam adds a significant contribution to the bay lateral strength, due to the vertical confinement exerted by the top beam deflection on the infill during the sway mechanism, which increases with the sliding joint friction resistance. On the other hand, the shear action overload in the column critical section due to the infill

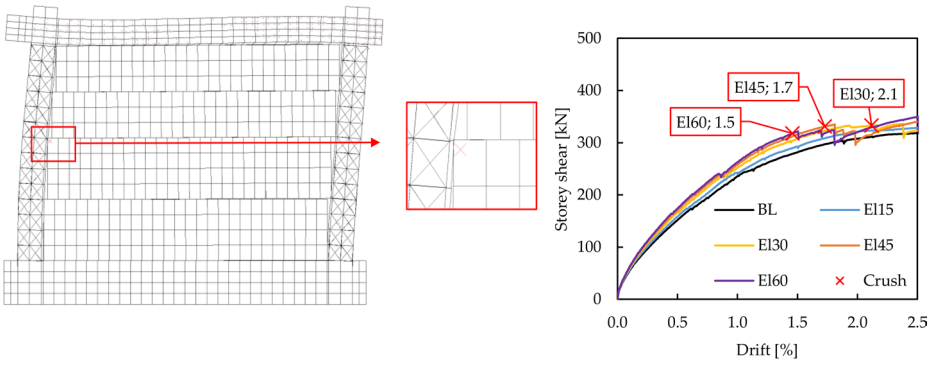

Fig. 19 Example of identification of the first crushing at the windward side of the second subpanel for the case study characterised by a stiffness of the lateral contact joints equal to 45 MPa and top gap (EL45) (**a**); report of the crushing activation occurring at drift values smaller than 2,5% for the ensemble of cases having different lateral contact joint stiffness and the top gap condition (**b**)

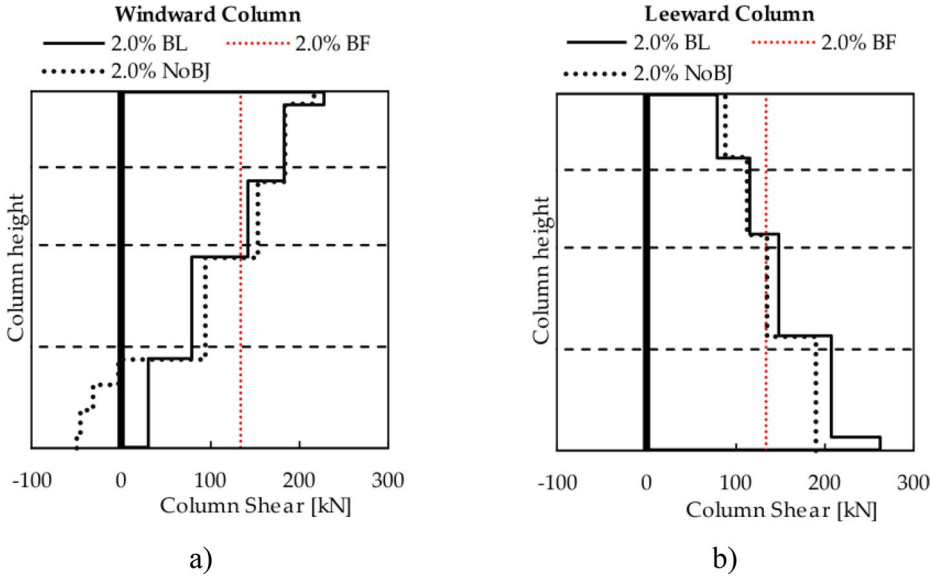

Fig. 20 Comparison of the shear profiles along the windward a) and leeward b) columns in the baseline model ("BL") and in the absence of the sliding joint at the base ("NoBJ") at a drift level equal to 2.0%. The shear action profile in the bare frame at 2,0% drift demand is also reported

interaction, V_{infill}, is slightly affected by the top contact layout: such overload in presence of a top contact joint, $V_{infill,top\text{-}joint}$, varies slightly with respect to the case with a top gap layout, $V_{infill,top\text{-}gap}$. For the analysed cases, the difference remained always below 20%, as reported in Table 5, and it does not significantly depend on the top joint stiffness, at least in the explored range of material properties.

The presence of plaster on the sliding joints adds an initial strength and stiffness that leads to an initial peak strength before the activation of the sliding. This initial peak strength may limit the initial damage of the infill, which can help to postpone the aesthetic cracking at the sliding joints for small earthquakes. However, the initial strength has to be limited to allow the triggering of the sliding joint mechanism, which is necessary to protect the structure from severe damage in stronger events.

The stiffness of the lateral contact joints slightly modifies the lateral strength, whilst it significantly affects the maximum shear overload in the columns, for both configurations with top joint and with top gap. The lateral contact joint stiffness governs the first local crushing at the corners of the subpanels and the shear action in the columns. As the stiffness increases, crushing is anticipated and the shear action in the columns increases. If the masonry sub-panel is sufficiently strong, local crushing may not occur, but that does not prevent from a higher interaction with the frame. Masonry properties of intermediate-to-high stiffness and weak compressive strength are more susceptible to anticipated corner crushing, as further discussed in the following.

In a design perspective, the infill damage could be preliminarily limited by controlling the ratio between the lateral contact joint stiffness, E_l, and the lateral compressive peak strength, f_{Mh}, of the masonry. A design proposal to protect the subpanel from corner crushing is derived in Eqs. 1 to 3, which limits the elastic modulus of the contact material as a function of the design target interstorey drift. Equation 3 is obtained by imposing a strength hierarchy along the contact length between the lateral contact joints and the masonry subpanels. Its derivation takes the following simplified assumptions: (i) the masonry of the subpanels is markedly stiffer than the contact material of the lateral contact joints, thus the relative rigid displacement of the masonry corner and adjacent column directly quantifies the lateral contact joint thickness reduction, Δ_s; (ii) a linear elastic constitutive law for the contact material of the lateral contact joint is assumed, with equivalent elastic modulus E_l ; (iii) the contact stress is assumed linearly proportional to the average strain of the contact material, obtained dividing Δ_s by the thickness, s_l, of the lateral contact material.

(Eq.1) quantifies the displacement Δ_s as in a pendular frame of rigid columns with pinned ends, where the contact area of the sub-panel to the lateral contact joint is equal to half of the subpanel height (Fig. 21). The maximum contact stress at the lateral contact joint,

Table 5 Effect of the presence of a top joint layout on the column end shear action overload ($V_{infill,top\text{-}joint}$) due to the infill local thrust, with respect to the top gap layout ($V_{infill,top\text{-}gap}$). The variation of the shear overload is quantified at four different drift values (0.5÷2.0%), for the windward top and leeward bottom column ends, for different values of the lateral contact joints material elastic modulus

Column Section	Drift	($V_{infill,top\text{-}joint}$ - $V_{infill,top\text{-}gap}$)/ $V_{infill,top\text{-}gap}$ Lateral contact joint elastic modulus (El)						Range of variation
		8 MPa (BL)	7.5 MPa	15 MPa	30 MPa	45 MPa	60 MPa	
windward top end	0.5	−14%	−14%	−7%	−3%	−1%	−1%	Max
	1.0	−11%	−11%	−1%	−4%	−3%	−2%	−1%
	1.5	−15%	−13%	−8%	−16%	−18%	−11%	Min
	2.0	−13%	−12%	−14%	−21%	−12%	−13%	−21%
leeward bottom end	0.5	17%	17%	16%	15%	17%	16%	Max
	1.0	12%	12%	13%	12%	12%	11%	18%
	1.5	18%	14%	15%	7%	7%	6%	Min
	2.0	14%	14%	11%	8%	5%	10%	5%

$\sigma_{c,lat}$, is thus quantified (Eq.2) as the product of the contact material average strain and the equivalent elastic modulus, E_l. Then, the upper limit for the ratio E_l over the masonry horizontal compressive strength, f_{Mh}, is obtained imposing $\sigma_{c,lat}$ lower than f_{Mh}. It is noteworthy that if the stiffness of the masonry and of the lateral contact material are comparable, the deformation of the masonry subpanel should not be neglected.

$$\Delta_s = \frac{\delta \cdot h}{2} \tag{1}$$

$$\sigma_{c,lat} = \frac{\delta \cdot h}{2} \cdot \frac{1}{s_l} \cdot E_l \tag{2}$$

$$\frac{E_l}{f_{Mh}} \leq \left(\frac{E_l}{f_{Mh}}\right)_{lim} = \frac{2 \cdot s_l}{\delta \cdot h} \tag{3}$$

Figure 22 compares the limit ratio $\left(\frac{E_l}{f_{Mh}}\right)_{lim}$ resulting from Eq.3 (applied to the BL case study geometry, $h = 730\,mm$ and $s_l = 25\,mm$) and the drift limit at the activation of the first crushing obtained numerically for the case studies analysed with different mechanical parameters (E_l, f_{Mh}). To test the proposal, a focus is made on the response of the AAC masonry type for different panels thicknesses, as it resulted the most vulnerable to corner crushing among the masonry types considered in the parametric study. Despite the simplification of its hypotheses, Eq.3 offers a safe-sided evaluation of the maximum lateral contact joint stiffness to avoid the corner crushing, for the case study under consideration.

5 Analytical interpretation

In the following, an analytical interpretation of the sliding joint infill response above described is presented, extending the formulation proposed in Preti et al. (2019) to take into consideration the specific elastic response of the lateral contact joint, without a cap yielding strength.

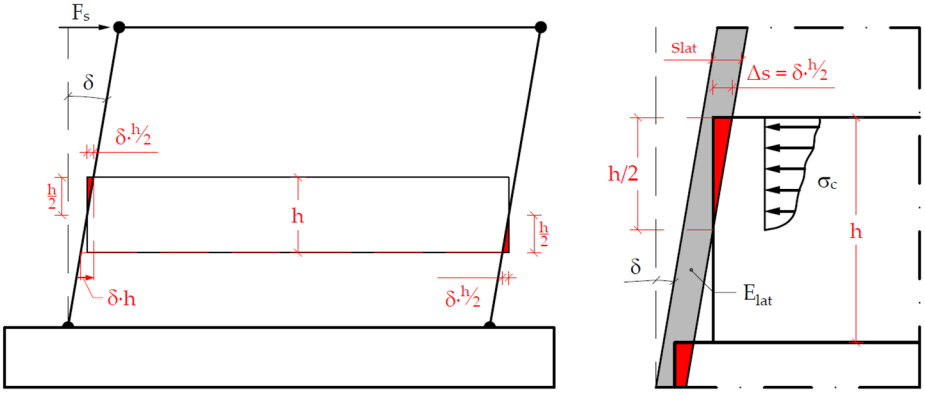

Fig. 21 Schematic representation of the distribution of the crushing between windward and leeward sides (left) and detail of the contact between the infill and the lateral contact joints (right)

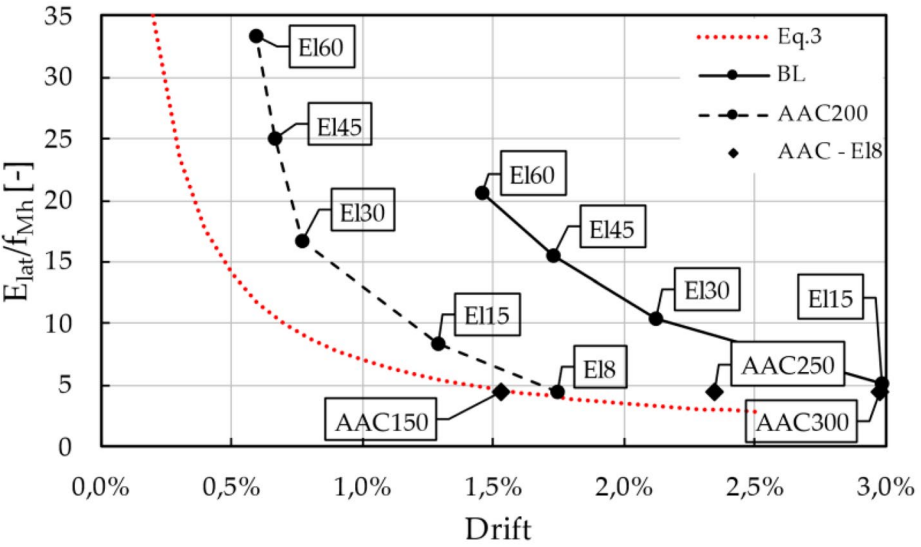

Fig. 22 Ratio of lateral contact joint stiffness over the masonry compressive stress as a function of the imposed interstorey drift at first crushing in the subpanel corner. Comparison of the values obtained by Eq. 3 and those of the most critical cases derived from the parametric analysis associated with the drift values where the first crushing of a subpanel corner is detected. Results for different values of lateral contact joint stiffness applied to the base line (BL) and AAC200 configurations. Detail of the role of infill thickness for the AAC infill with constant lateral contact joint stiffness (AAC – El8)

The approach considers the superposition of the effects of the infill and of the bare frame: the contribution of the infill is individually evaluated, referring to a pendular frame with rigid elements, and it is subsequently added to that of the bare frame. The prediction of the lateral interstorey strength versus drift of the infill is meant to allow for the calibration of a strut macro-model, explicitly accounting for the infill contribution in the numerical analysis of multi-storey frame structures. Moreover, the prediction of the shear internal action induced by the infill thrust on the columns, as a function of the interstorey drift, allows both for the column proportioning and for the a-posteriori column shear check.

The proposed analytical model is built for infills characterised by the baseline model layout discussed in the previous section: horizontal sliding joints at the infill base and between the sub-panels, and top gap. The alternative detailing introduced in the reference experimental test above discussed can be interpreted by comparison to the results of the baseline layout. The choice is justified to take advantage of the simplification resulting with the baseline configuration. In particular, one of the advantages of the baseline configuration is that the contact forces acting along the height of the columns have similar intensity (Fig. 23a); without the base joint, instead, high concentration occurs at the windward side of the first subpanel, and no contact force is exerted at the base of the leeward side, resulting in an irregular distribution of the contact forces (Fig. 23b), which are difficult to quantify. Furthermore, with the top gap the model can disregard the stress transfer from the top beam, which should be otherwise accounted for if the top joint has non-negligible stiffness.

The analytical model quantifies the infill contribution by considering an ideal pendular system subjected to the horizontal ($R_{h,i}$) and vertical ($R_{v,i}$) contact forces acting along the

columns (Fig. 24a). The shear action at the top of the windward V_{top}^{Win} and leeward V_{top}^{Lee} columns are derived by imposing the rotational equilibrium at the base of the columns (Eqs. 4 and 5). The algebraic sum of the two column-top-end shear actions gives the contribution of the infill to the bay lateral strength (Eq. 6).

The distributed contact forces along the columns are simplified by evaluating their horizontal $R_{h,n}$ and vertical $R_{v,n}$ resultants at each subpanel (Fig. 24b), according to two mechanisms: (i) a diagonal "strut" inside each subpanel and (ii) a "friction" mechanism between them (Fig. 25). In the analytical model, some simplifying hypotheses have been assumed, such as uniform subpanel heights, contact heights, and contact forces. The efficiency of the simplified assumptions is evaluated by comparing the infill lateral strength and column shear actions so predicted with the values derived from Eqs. 4 to 6 using the numerical model contact forces.

$$V_{top}^{Win} = \frac{1}{H} \cdot \sum_{i=1}^{N} \left[R_{h,i}^{Win} \cdot Z_i + \frac{1}{2} R_{v,i}^{Win} \cdot b_c \right] \tag{4}$$

$$V_{top}^{Lee} = -\frac{1}{H} \cdot \sum_{i=1}^{N} \left[R_{h,i}^{Lee} \cdot Z_i - \frac{1}{2} R_{v,i}^{Lee} \cdot b_c \right] \tag{5}$$

$$F_s = V_{top}^{Win} + V_{top}^{Lee} \tag{6}$$

The strut mechanism assumes a strut per each subpanel, oriented along the diagonal, and no friction along the sliding joints. Accordingly, the horizontal component of the contact forces at the leeward and windward sides has same resultant, by equilibrium. If the contact material

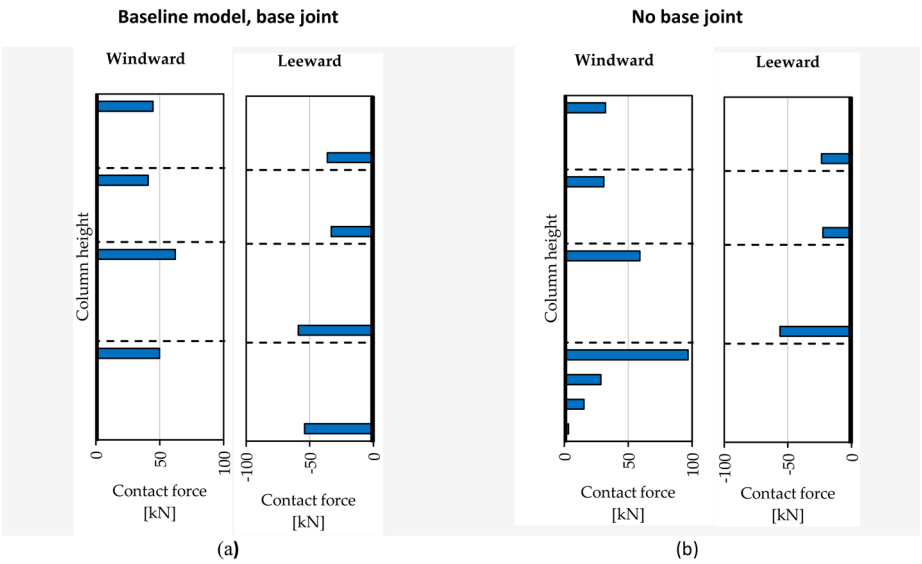

Fig. 23 Comparison of the contact forces horizontal component along the windward and leeward columns in the baseline model (**a**) and in the absence of the sliding joint at the base (**b**), at an interstorey drift level equal to 2.0%

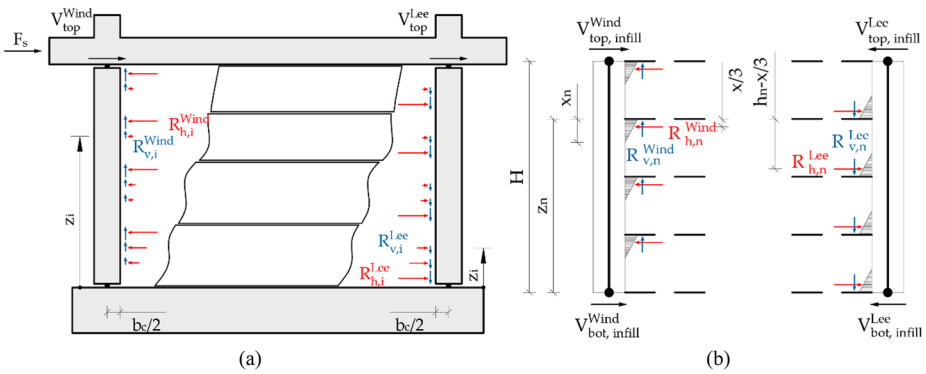

Fig. 24 Frame pendular layout with the description of the column contact force distribution quantified from the numerical model (subscript "i" refers to the single interface element reaction) (**a**); static scheme assumed in the equilibrium equations of the windward and leeward columns starting from the equivalent resultant contact forces (subscript "n" refers to the single subpanel)

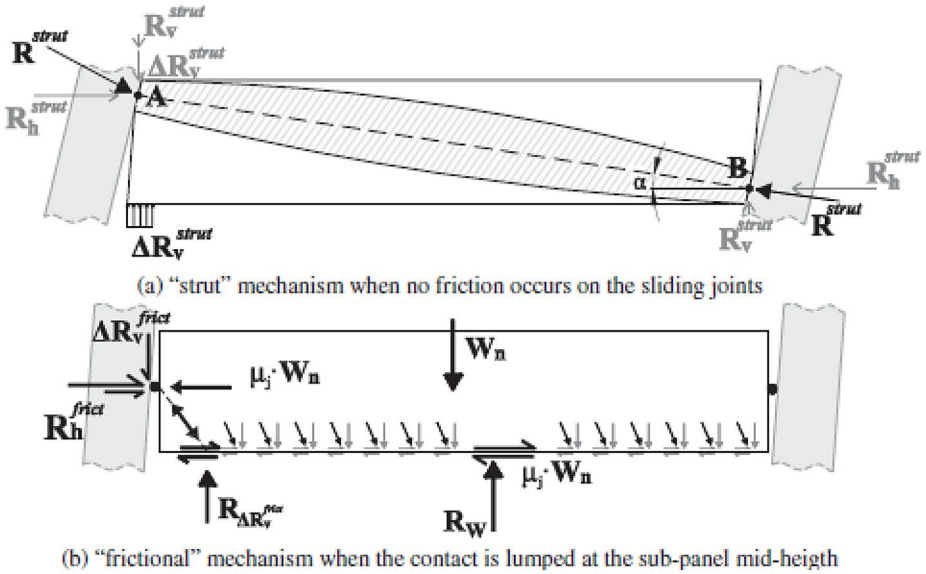

Fig. 25 Static scheme at the base of the analytical formulation proposed in Preti et al. (reprinted from Preti et al. 2019). The column contact forces are interpreted as the superposition of strut mechanism along the sub-panel diagonal (**a**) and a frictional mechanism in between subpanels (**b**)

undergoes yielding (Preti et al. 2019), the horizontal component of the contact force, $R_{h,n}^{strut}$, is derived by integrating a simplified stress block distribution of the contact stresses as in Eq. 7, assuming the mobilisation of the compressive strength of the contact material σ_c. In Eq. 7, β is the stress block factor to quantify the equivalent contact depth, assumed equal to 0.8, t is the lateral contact joint effective depth, and $\bar{X}_n^{Lee}$ is the contact length. The vertical component on the leeward side $R_{v,n}^{strut,Lee}$ is calculated from the horizontal one, assuming an inclination of the contact force equal to the sub-panel diagonal α (Eq. 8). On the windward side, if relative sliding between the lateral contact joint and the subpanel is expected to occur, the vertical component $R_{v,n}^{strut,Win}$ is derived from the horizontal one by applying the friction coefficient μ_c of the vertical joint (Eq. 9).

$$R_{h,n}^{strut} = \beta \cdot t \cdot \bar{X}_n^{Lee} \cdot \sigma_c \tag{7}$$

$$R_{v,n}^{strut,Lee} = R_{h,n}^{strut} \cdot \tan(\alpha) \tag{8}$$

$$R_{v,n}^{strut,Win} = R_{h,n}^{strut} \cdot \mu_c \tag{9}$$

If the lateral contact joint has an elastic response without a yielding stress cap, the contact stresses progressively increase with the imposed inter-storey drift. A strategy to quantify the stress variation with a rational approximation assumes a linear strain profile of the lateral contact joints along the contact length. A joint thickness reduction, $_s$, proportional to the local drift, δ, and to the distance from the neutral axis is quantified. Then the horizontal contact stress is obtained by multiplying the average strain calculated in the joint thickness, s_l, by the lateral contact joint modulus of elasticity, E_l. The maximum contact stress, $\sigma_{c,max}$, as a function of the drift is thus quantified by Eq. 10, with the only unknown of the contact depth. In Sect. 4, a safe-sided contact depth equal to half of the subpanel height was roughly derived from geometrical considerations, assuming the deformation of the contact material in between the sub-panel and columns rigidly moving. In this case, a more detailed estimation is required to represent the contact depth variation as a function of the imposed drift, the column deflection and the subpanel deformation, as described in the following section. The horizontal component of the contact force at the leeward side, $R_{h,n}^{strut}$, is then quantified by Eq. 11.

$$\sigma_{c,max} = \frac{\delta \cdot \bar{X}_n^{Lee}}{s_l} \cdot E_l \tag{10}$$

$$R_{h,n}^{strut} = 0.5 \cdot t \cdot \bar{X}_n^{Lee} \cdot \frac{\delta \cdot \bar{X}_n^{Lee}}{s_l} \cdot E_l \tag{11}$$

According to the above simplifications, Eqs. 4 and 5 specify into Eqs. 12 and 13, where ψ is equal to 0.8 for a plastic contact material, while it is equal to 2/3 for an elastic contact material, according to a linear distribution of the contact stresses (Fig. 24b). b_c is the column in-plane depth and H is the bay height.

$$V_{top}^{Win} = \frac{1}{H} \cdot \sum_{n=1}^{N} \left[R_{h,n}^{Win} \cdot \left(Z_n - \frac{\psi}{2} \cdot \bar{X}_n^{Win} \right) + \frac{1}{2} R_{v,n}^{Win} \cdot b_c \right] \tag{12}$$

$$V_{top}^{Lee} = -\frac{1}{H} \cdot \sum_{n=1}^{N} \left[R_{h,n}^{Lee} \cdot \left(Z_n - h_n + \frac{\psi}{2} \cdot \bar{X}_n^{Lee} \right) - \frac{1}{2} R_{v,n}^{Lee} \cdot b_c \right] \tag{13}$$

In case of uniform sub-panel height, $h = H/N$, contact length, $\bar{X}^{Lee}$, and contact forces, $R_{h,n,,ave}^{Strut}$, Eqs. 14, 15, and 16 can be derived, describing the shear acting at the top of the columns and the lateral strength as a result of the strut mechanism. The angle θ_w describes the inclination of the contact force at the windward side, whose calibration is discussed in the following section, while N is the number of the subpanels.

$$V_{top}^{Strut,Win} = R_{h,n,ave}^{Strut} \cdot \left[\frac{N+1}{2} - \frac{\psi}{2} \left(\frac{\bar{X}^{Lee}}{h} \right) + \frac{\tan(\theta_w) \cdot b_c}{2h} \right] \tag{14}$$

$$V_{top}^{Strut,Lee} = -R_{h,n,ave}^{Strut} \cdot \left[\frac{N-1}{2} + \frac{\psi}{2} \left(\frac{\bar{X}^{Lee}}{h} \right) - \frac{\tan(\alpha) \cdot b_c}{2h} \right] \tag{15}$$

$$\Delta F_s^{Strut} = V_{top}^{Strut,Win} + V_{top}^{Strut,Lee} = R_{h,n,ave}^{strut} \cdot \left[\left(1 - \psi \cdot \frac{\bar{X}^{Lee}}{h} \right) + \frac{b_c}{2h} (\tan(\theta_w) - \tan(\alpha)) \right] \tag{16}$$

On the windward side, the contribution of the friction mechanism to the shear at the top of the column (Preti et al. 2019) must be added as described by Eq. 17, where W is the self-weight of the subpanels and μ_j is the friction coefficient of the sliding joints. Note that the contribution of the infill self-weight in Eq.17 is typically small and can thus be neglected.

$$V_{top}^{fricti,Win} = \frac{1}{2} \cdot \left[W + N \cdot R_{h,n,ave}^{strut} \cdot (\tan(\theta_w) - \tan(\alpha)) \right] \cdot \left(\frac{1}{1 - \mu_j \tan(\theta_w)} \right) \cdot \mu_j \tag{17}$$

$$V_{top}^{Win} = V_{top}^{Strut,Win} + V_{top}^{fricti,Win} \tag{18}$$

The total contribution of the infill to the bay lateral strength is given by the sum of Eqs. 16 and 17 into Eq. 18. The maximum shear action in the columns occurs at the windward top and leeward bottom cross-sections. In both cases the effect of the infill can be quantified with good approximation by Eq. 18 as the sum of the contributions quantified by Eqs. 14 and 17.

The maximum shear action on the frame columns can be derived by superposing the shear action induced by the infill thrust to that measured on the bare frame for the target drift level.

It is noteworthy that the proposed formulations are calibrated for a lateral contact joint of elastic contact material, 25 mm thickness and elastic modulus varying in the range of 7.5 to 60 MPa, for drift level up to 2.5%.

5.1 Calibration of the contact depth and of the inclination of the contact forces

The previously described formulations require the calibration of the contact depth on the leeward side, $\bar{X}^{Lee}$, and the evaluation of the inclination of the contact force on the windward side, θ_w. Such two parameters are here quantified based on the results of the parametric analysis described in Sect. 3.

As in the original formulation (Preti et al. 2019), the contact depth $\bar{X}^{Lee}$ is empirically calibrated from the average numerical contact force acting on the leeward column. In the presence of a yielding contact material the original work quantifies the average contact length with Eq. 19.

$$\begin{cases} \bar{X}^{Lee} = h \cdot [0.3 - 0.019 \cdot (N-4)] \cdot \delta\,(\%)\,, \delta \leq 1\% \\ \bar{X}^{Lee} = h \cdot \left[0.3 \cdot \sqrt[3]{\delta\,(\%)} - 0.019 \cdot (N-4)\right], \delta > 1\% \end{cases} \tag{19}$$

In the presence of an elastic contact material, the numerical contact depth $\bar{X}^{Lee}_{num}$ is here derived from the average contact force $R_{h,mean}$ by rewriting Eq. 11 into Eq. 20.

$$\bar{X}^{Lee}_{num} = \sqrt{\frac{2 \cdot R_{h,mean} \cdot s_l}{t \cdot E_l \cdot \delta\,(\%)\,/100}} \tag{20}$$

The analytical fit, $\bar{X}^{Lee}_{an}$, of the results of the parametric study can be obtained with Eq. 21, having a negative exponential dependence with the elastic modulus of the contact material E_l (in MPa) and a linear dependence with the inter-storey drift, $\delta\,(in\%)$ (Fig. 28a).

$$\bar{X}^{Lee}_{an} = h \cdot E_l^{-0.37}\,(0.95 - 0.1 \cdot \delta) \tag{21}$$

The vertical component of the contact forces on the windward side can be evaluated from the friction μ_c of the infill-to-contact material interface, if sliding is expected. In the presence of a contact material with a low shear stiffness, as considered in this work, the shear deformability may prevent the sliding, as shown by the numerical results. The inclination of the contact forces at the windward side can be expected to be limited within the inclination of the subpanel diagonal, α, (similarly as at the leeward side) and the angle corresponding to the friction coefficient of the infill-to-lateral contact joint interface, μ_c (Fig. 26b).

The analytical assessment of such an inclination is non-trivial since the compatibility of the displacements at the lateral contact joints must be considered. In the present study, the inclinations of the contact forces at the windward and leeward column interfaces are numerically evaluated as the average ratio of the vertical and horizontal components of the numerical contact forces on the different sub-panels. The results are reported in Fig. 26b. By varying the elastic stiffness of the contact material, the results show that the inclination at the leeward side (dashed lines) remains close to the inclination of the subpanel diagonal, while at the windward side (continuous line), it is higher, and it varies from a minimum value of about 0.36 for the baseline case to 0.6 for the stiffer case.

The inclination of the strut at the windward side could be represented by an exponential expression, but a simpler linear relationship with the elastic stiffness of the lateral contact material is proposed (Eq. 22). The proposal (dotted lines) is compared to the numerical results in Fig. 26b. Note that numerical result data are disregarded starting from a stiffness of 30 MPa for drift larger than 1.5%; here the sudden drop corresponds to the local crushing of the masonry after which the redistribution of stresses does not allow for a clear reading of the strut inclination.

$$\tan\,(\theta_w) = 0.3 + 0.005 E_l\,(MPa) \tag{22}$$

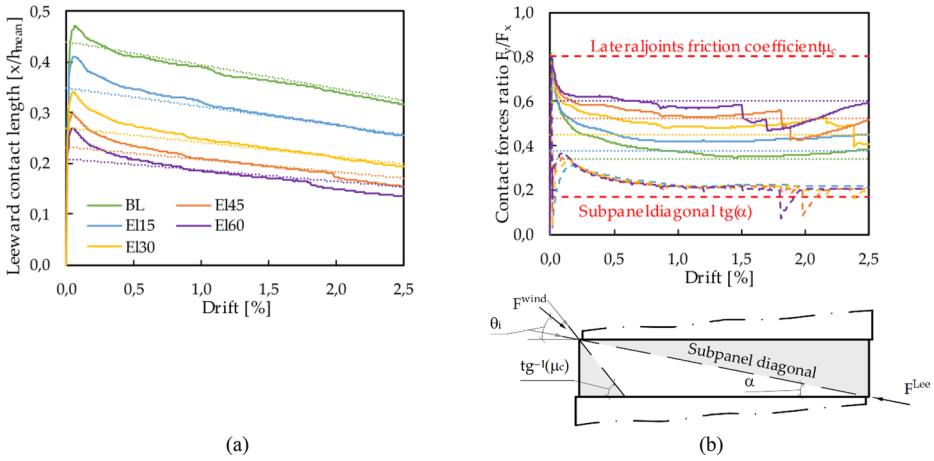

Fig. 26 **a**) Comparison of the proposed contact depth at the leeward side (dotted line) with the numerical one (continuous line) for different stiffnesses of the lateral contact joints. **b**) schematic of the range of the strut inclination and quantification in terms of ratio between the resultant of the vertical and horizontal component of the contact forces at the windward (continuous) and leeward (dashed) columns. The ratio is expressed as a function of the interstorey drift and for different values of the elastic stiffness of the lateral contact joint contact material. The lower (tangent of the subpanel diagonal) and upper (friction at the lateral contact joints) limits are also represented together with the empirical prediction at the windward side obtained by Eq. 22 (dotted line)

5.2 Validation of the analytical model

Figures 27 and 28 compare the prediction (dotted lines) of the infill contribution to the lateral strength (Fig. 27),of the normalised contact depth (Fig. 28a), of the sum of the horizontal contact forces (Fig. 28b), and of the shear actions overload in the columns (Fig. 28c and d) to the numerical results of the baseline model (continuous lines). An overall good agreement between the results is shown. Figure 29 shows the comparison for the shear action at the top of the windward column and for the infill lateral strength when varying the lateral contact joint stiffness and infill bay length, respectively. The results show a good match except after the local crushing of the subpanel corners at high drift levels for large values of the elastic modulus, as previously explained.

Given the empirical calibration of the contact depth and of the inclination of the contact forces at the windward side, the analytical model applies within the limitations of the case studies adopted in this work.

6 Conclusions

The paper collects the results of a numerical parametric analysis on the local interaction between the RC frame and the innovative masonry infills with sliding joints, in infilled frame structures. A well-established finite element modelling approach through detailed FEMs is adopted, with parameters calibrated with the data from a previous experimental campaign. Design equations are proposed, derived by extending a previously developed analytical model, with the aim of incorporating them into practical design guidelines. The

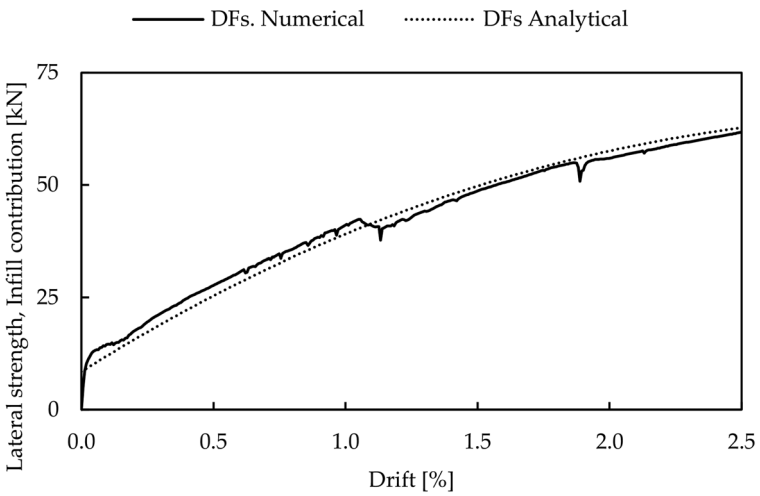

Fig. 27 Comparison of the numerical and analytical contribution of the infill to the lateral strength evaluated for the baseline model (BL) as a function of the interstorey drift

equations predict the lateral strength contribution and the column shear overload due to the infill frame interaction and are validated against two different experimental campaigns on similar types of infill with sliding joints. The extension of the analytical equation here presented accounts for the role of a column-to-infill contact material characterized by an elastic response of low stiffness, an alternative to previously tested elastic-plastic contact material solutions. The influence of the infill-frame contact material stiffnesses is analysed together with other design parameters, such as the RC frame bay length, the infill masonry properties, the layout of sliding joints and the characteristics of lateral and top contact joints.

The parametric analysis shows the importance of some investigated construction details and highlights some design implications, summarized as follows.

- Regarding the preferable number of sub-panels separated by sliding joints, three sub-panels (i.e., two sliding joints) resulted sufficient to obtain a ductile response, while a minimum of four (i.e., three sliding joints) is required to postpone the masonry crushing after 2.5% drift. More than four sub-panels do not significantly improve the in-plane behaviour.
- A uniform height for the sub-panels showed its efficiency, even if little differences between subpanels do not significantly affect the response.
- The presence of a sliding joint at the base of the infill does not significantly modify the global response of the infilled frame, but it modifies the distribution of the shear action between the columns: without the sliding joint at the base a beneficial reduction of the peak shear load in the leeward column occurs.
- The contact joint between the infill and the bay top beam adds a contribution to the bay lateral strength, due to the vertical confinement exerted by the top beam on the infill in the sway mechanism. Such top contact joint increases also the shear action on the columns, with an increment up to 20% (in the range of explored parameters) compared to the configuration with a top gap instead of the contact joint.

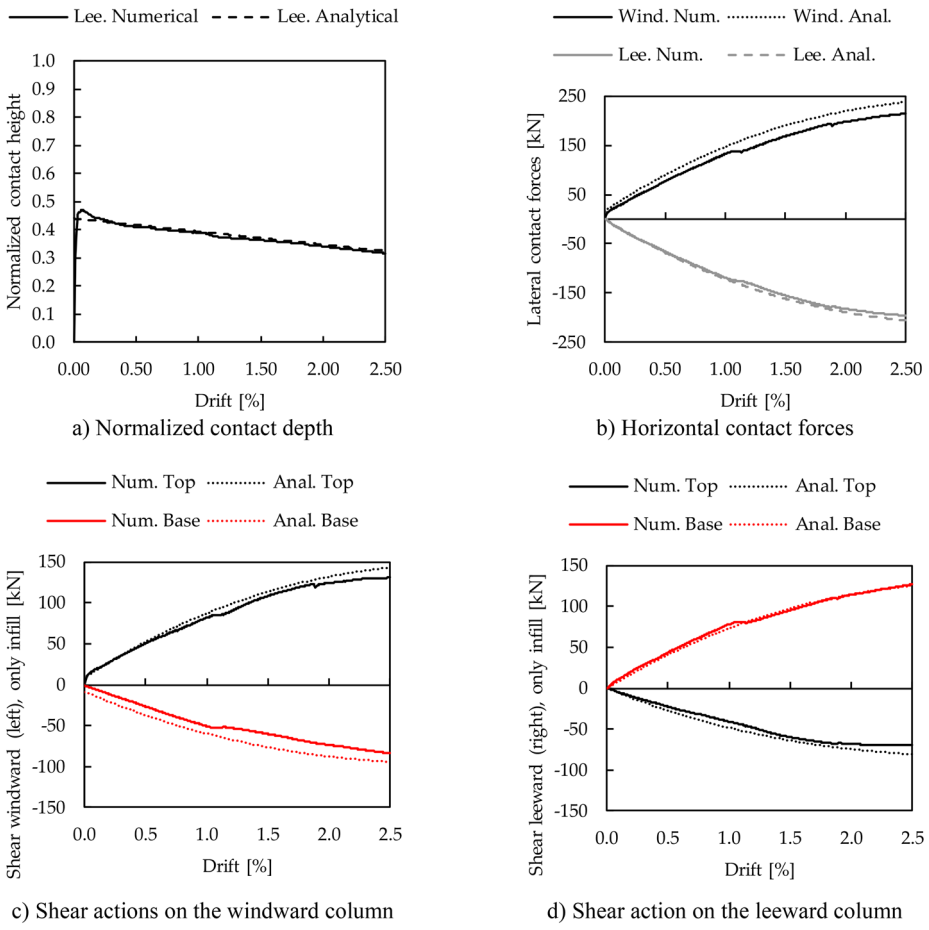

Fig. 28 Comparison of the numerical (continuous lines) and analytical (dotted lines) evaluations of the normalized average contact depth, horizontal contact forces, and column shear action overload due to the infill-frame interaction, quantified for the baseline model (BL) as a function of the interstorey drift

- The presence of plaster on the sliding joints adds an initial strength and stiffness that leads to an initial peak of strength before the activation of the sliding. This initial peak strength may limit the initial damage of the infill and may help to postpone the aesthetic cracking at the sliding joints for small earthquakes. However, the initial strength should be limited to allow the triggering of the sliding joint mechanism, which is necessary to protect the structure from severe damage in stronger events.
- The stiffness of the lateral infill-column contact joints slightly modifies the lateral infilled frame strength but significantly affect the maximum shear overload in the columns, for both configurations with top contact joint and top gap. The structural response results practically insensitive to the infill length and the masonry mechanical properties, in the range of explored parameters.
- In a design perspective, the infill damage could be preliminarily limited by controlling the ratio between the lateral contact joint stiffness and thickness $(E_l; s_l)$ and the lateral

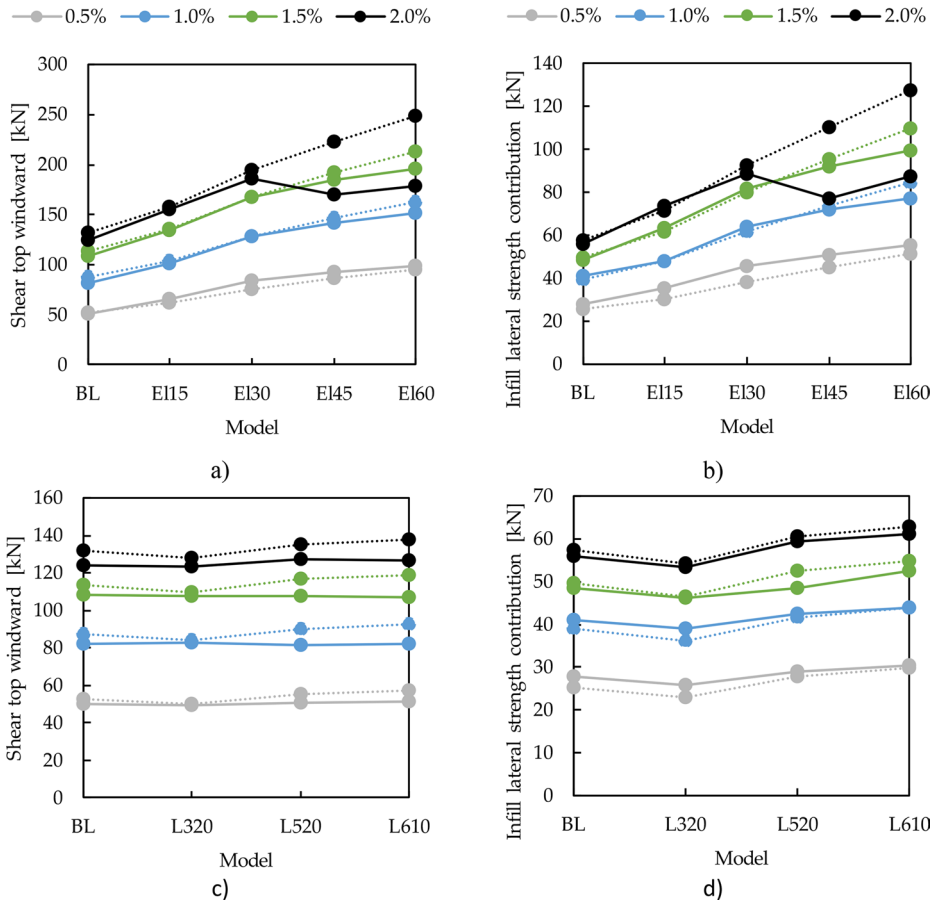

Fig. 29 Comparison of the numerical (continuous lines) and analytical (dotted lines) evaluation of the shear action at the top of the windward column and of the infill contribution to the lateral strength quantified for the base line model layout (BL) varying the stiffness of the lateral contact joints (**a,b**) or the infill bay length (**c,d**)

compressive peak strength (f_{Mh}) of the masonry. A design equation to protect the sub-panel from corner crushing is proposed.

- The analytical interpretation of the sliding joint infill response proposed in Preti et al. (2019) is here extended to take into consideration an elastic response, with no cap yielding strength, of the lateral contact joint. The proposed equations provide good match with the numerical results. The prediction of the infill contribution in terms of "lateral strength versus drift" is meant to allow for the calibration of a strut macro-model to explicitly account for the infill contribution in the numerical analysis of multi-storey frame structures. The prediction of the additional shear internal action induced by the infill thrust on the columns, as a function of the inter-storey drift, allows both for the column proportioning and for the a-posteriori column shear check.

The studied infill typology can be classified as "interacting ductile" according to Italian NTC18 (2018) and the latest draft of EC8-1–2 (CEN 2025)). However, the provided equations allow to explicitly quantify the intensity of the infill-frame interaction and to justify their possible classification as "non-interacting" infills depending on the code requirement evolution. Regarding the in-plane response of ductile infills, prEC8 1–2 specifies interstorey drift limits of 0.50%, 1.25%, and 2.20% for the operational, damage limitation, and severe damage states, respectively, although for ductile infills with horizontal sliding joints, as the ones here considered, the drift capacities corresponding to the damage limitation and severe damage states may be significantly larger when infill detailing is accurately designed.

Acknowledgements The experimental campaign presented in this work was conducted at the University of Pavia and Eucentre Foundation thanks to the financial support of the European Commission within the project INSYSME "INnovative SYStems for earthquake resistant Masonry Enclosures in rc buildings", grant FP7-SME-2013-2-GA606229, 2013-2016. The numerical part and the study of the local effects were carried out within the framework of DPC/ReLUIS project 2022–2024 and 2024-2026, WP10, where researchers from the University of Brescia and the University of Pavia were involved.

Author contributions All authors contributed to the study conception and design. The test campaign was performed by Riccardo Milanesi, Paolo Morandi and Guido Magenes of the research group of the University of Pavia and Eucentre. The numerical study was performed by Simone Pelucco, Valentino Bolis and Marco Preti of the research group of the University of Brescia with the support of Andreas Stavridis of the University at Buffalo. The first draft of the manuscript was written by Simone Pelucco and Riccardo Milanesi and all authors commented on previous versions of the manuscript. Supervision: Marco Preti. All authors read and approved the final manuscript.

Funding Open access funding provided by Università degli Studi di Brescia within the CRUI-CARE Agreement. The experimental campaign presented in this work was conducted at the University of Pavia and Eucentre Foundation thanks to the financial support of the European Commission within the project INSYSME "INnovative SYStems for earthquake resistant Masonry Enclosures in rc buildings", grant FP7-SME-2013-2-GA606229, 2013-2016. The numerical part and the study of the local effects were carried out within the framework of DPC/ReLUIS project 2022-2024, WP10, where researchers from the University of Brescia and the University of Pavia were involved.

Data availability Not applicable

Declarations

Competing interests The authors have no relevant financial or non-financial interests to disclose.

References

Binici B, Canbay E, Aldemir A, Demirel IO, Uzgan U, Eryurtlu Z, Bulbul K, Yakut A (2019) Seismic behavior and improvement of autoclaved aerated concrete infill walls. Eng Struct 193:68–81. https://doi.org/10.1016/j.engstruct.2019.05.032

Bolis V, Stavridis A, Preti M (2017) Numerical investigation of the in-plane performance of masonry-infilled RC frames with sliding subpanels. J Struct Eng 143(2):04016168. https://doi.org/10.1061/(ASCE)ST.1943-541X.0001651

Bose S, Martin J, Stavridis A (2019) Simulation framework for infilled RC frames subjected to seismic loads. Earthquake Spectra 35(4):1739–1762. https://doi.org/10.1193/042218EQS100M

CEN (2004) Eurocode 2: design of concrete structures, EN 1992-1-1:2004. European Committee for Standardization, Brussels, Belgium

CEN (2025) Eurocode 8 - design of structures for earthquake resistance, Part 1-2. Buildings, FprEN1998-1-2. 2025, CEN/TC 250/SC 8 N 1396. European Committee for Standardisation, Brussels, Belgium

Cheng X, Zou Z, Zhu Z, Zhai S, Yuan S, Mo Y, Chen W, He J (2020) A new construction technology suitable for frame partitioned infill walls with sliding nodes and large openings: test results. Construct Building Mater 258:119644. https://doi.org/10.1016/j.conbuildmat.2020.119644

D.M. 17/01/2018 (2018) Norme Tecniche per le Costruzioni (NTC18), Gazzetta Ufficiale n. 42 del 20/02/2018, Supplemento ordinario n.8 (in Italian)

Fikri R, Dizhur D, Walsh K, Ingham J (2019) Seismic performance of reinforced concrete frame with masonry infill buildings in the 2010/2011 Canterbury, New Zealand earthquakes. Bull Earthquake Eng 17(2):737–757. https://doi.org/10.1007/s10518-018-0476-8

Fragomeli A, Galasco A, Graziotti F, Guerrini G, Kallioras S, Magenes G, Malomo D, Mandirola M, Manzini CF, Marchesi B, Milanesi RR, Morandi P, Penna A, Rossi A, Rosti A, Rota M, Senaldi I, Tomassetti U, Cattari S, da Porto F, Sorrentino L (2017) Comportamento degli edifici in muratura nella sequenza sismica dell'Italia centrale del 2016 - Parte, 1: Quadro generale (in Italian). Progett Sismica 8(2):49–77

Furtado A, Rodrigues H, Arêde A, Melo J, Varum H (2021) The use of textile-reinforced mortar as a strengthening technique for the infill walls out-of-plane behaviour. Compos Struct 255:113029. https://doi.org/10.1016/j.compstruct.2020.113029

Gao X, Stavridis A, Bolis V, Preti M (2018) Experimental study on the seismic performance of non-ductile RC frames infilled with sliding subpanels. In: Proceedings of the Eleventh U.S. National Conference on Earthquake Engineering Integrating Science, Engineering & Policy, June 25–29, 2018, Los Angeles, California

Gao X, Stavridis A, Bolis V, Preti M (2024) Overview of an experimental investigation of the seismic performance of non-ductile RC frames with new and existing masonry infills with sliding subpanels. In: Proceedings of the 18th World Conference on Earthquake engineering, WCEE2024, June 30th - July 5th 2024, Milan, Italy

Koutromanos I, Stavridis A, Shing B, Willam K (2011) Numerical modeling of masonry-infilled RC frames subjected to seismic loads. Comput Struct 89(11–12):1026–1037. https://doi.org/10.1016/j.compstruc.2011.01.006

Lotfi HR, Shing PB (1991) An appraisal of smeared crack models for masonry shear wall analysis. Comput Struct 41(3):413–425. https://doi.org/10.1016/0045-7949(91)90134-8

Mander JB, Priestley MJN, Park R (1988) Theoretical stress-strain model for confined concrete. J Struct Eng 114(8):1804–1826. https://doi.org/10.1061/(ASCE)0733-9445(1988)114:8(1804)

Manzini CF, Morandi P (2012) Rapporto preliminare sulle prestazioni ed i danneggiameti agli edifici in muratura portante moderni a seguito degli eventi sismici emiliani del 2012 (in Italian), Eucentre, https://www.eqclearinghouse.org/2012-05-20-italy/

Marinkovic M, Butenweg C (2019) Innovative decoupling system for the seismic protection of masonry infill walls in reinforced concrete frames. Eng Struct 197:109435. https://doi.org/10.1016/j.engstruct.2019.109435

Mehrabi AB, Shing PB (1997) Finite element modeling of masonry-infilled RC frames. J Struct Eng 123(5):604–613. https://doi.org/10.1061/(ASCE)0733-9445(1997)123:5(604)

Milanesi RR (2016) Seismic performance of a newly conceived masonry infill with sliding joints. In: Ph.D Thesis in Earthquake Engineering and Engineering Seismology, Scuola Universitaria Superiore IUSS Pavia, Italy, December 2016

Milanesi RR, Morandi P, Dacarro F, Albanesi L, Magenes G (2017) In-plane cyclic and out-of-plane dynamic testing procedures for infilled RC frames. In: Proc. 7AESE, Pavia, Italy, 6–8 September 2017

Milanesi RR, Morandi P, Manzini CF, Albanesi L, Magenes G (2022) Out-of-plane response of an innovative masonry infill with sliding joints from shaking table tests. J Eart Eng 26(4):1789–1823. https://doi.org/10.1080/13632469.2020.1739173

Morandi P, Milanesi RR, Magenes G (2018) Innovative solution for seismic-resistant masonry infills with sliding joints: in-plane experimental performance. Eng Struct 176:719–733. https://doi.org/10.1016/j.engstruct.2018.09.018

Parisi F, De Luca F, Petruzzelli F, De Risi R, Chioccarelli E, Iervolino I (2012) Field inspection after the May 20th and 29th 2012 Emilia-Romagna Earthquakes, available at http://www.reluis.it

Pohoryles DA, Bournas DA (2020) Seismic retrofit of infilled rc frames with textile reinforced mortars: state-of-the-art review and analytical modelling. Compos Part B 183:107702. https://doi.org/10.1016/j.compositesb.2019.107702

Preti M (2024) Deformable masonry infills: a state-of-the-art review. In: Proceedings of the 18th World Conference on Earthquake engineering, WCEE2024, June 30th - July 5th 2024, Milan, Italy

Preti M, Bettini N, Plizzari G (2012) Infill walls with sliding joints to limit infill-frame seismic interaction: large-scale experimental test. J Eart Eng 16(1):125–141. https://doi.org/10.1080/13632469.2011.579815

Preti M, Bolis V (2017) Masonry infill construction and retrofit technique for the infill-frame interaction mitigation: test results. Eng Struct 132:597–608. https://doi.org/10.1016/j.engstruct.2016.11.053

Preti M, Bolis V, Stavridis A (2019) Seismic infill–frame interaction of masonry walls partitioned with horizontal sliding joints: analysis and simplified modeling. J Eart Eng 23(10):1651–1677. https://doi.org/10.1080/13632469.2017.1387195

Preti M, Migliorati L, Giuriani E (2015) Experimental testing of engineered masonry infill walls for post-earthquake structural damage control. Bull Earthquake Eng 13(7):2029–2049. https://doi.org/10.1007/s10518-014-9701-2

Redmond L, Ezzatfar P, DesRoches R, Stavridis A, Ozcebe G, Kurc O (2016) Finite element modeling of a reinforced concrete frame with masonry infill and mesh reinforced mortar subjected to earthquake loading. Earthquake Spectra 32(1):393–414. https://doi.org/10.1193/081314EQS128M

Stavridis A (2009) Analytical and experimental study of seismic performance of reinforced concrete frames infilled with masonry walls. PhD thesis. Department of Structural Engineering, University of California, San Diego, CA

Stavridis A, Shing PB (2010) Finite-element modeling of nonlinear behavior of masonry-infilled RC frames. J Struct Eng 136(3):285–296. https://doi.org/10.1061/(ASCE)ST.1943-541X.116

Taylor RL (2007) FEAP - A finite element analysis program - user manual, Dept. of Civil and Environmental Engineering. University of California, Berkeley, CA, pp 705

Totoev YZ, Al Harthy A (2016) Semi interlocking masonry as infill wall system for earthquake resistant buildings: a review. Jou Eng Res 15(2):33–41. https://doi.org/10.24200/tjer.vol13iss1pp33-41

Valluzzi MR, da Porto F, Garbin E, Panizza M (2014) Out-of-plane behaviour of infill masonry panels strengthened with composite materials. Mater Struct 47(12):2131–2145. https://doi.org/10.1617/s11527-014-0384-6

Verderame GM, Balsamo A, Ricci P, Di Domenico M, Maddaloni G (2019) Experimental assessment of the out-of-plane response of strengthened one-way spanning masonry infill walls. Compos Struct 230:111503. https://doi.org/10.1016/j.compstruct.2019.111503